



저작자표시-비영리-변경금지 2.0 대한민국

이용자는 아래의 조건을 따르는 경우에 한하여 자유롭게

- 이 저작물을 복제, 배포, 전송, 전시, 공연 및 방송할 수 있습니다.

다음과 같은 조건을 따라야 합니다:



저작자표시. 귀하는 원저작자를 표시하여야 합니다.



비영리. 귀하는 이 저작물을 영리 목적으로 이용할 수 없습니다.



변경금지. 귀하는 이 저작물을 개작, 변형 또는 가공할 수 없습니다.

- 귀하는, 이 저작물의 재이용이나 배포의 경우, 이 저작물에 적용된 이용허락조건을 명확하게 나타내어야 합니다.
- 저작권자로부터 별도의 허가를 받으면 이러한 조건들은 적용되지 않습니다.

저작권법에 따른 이용자의 권리는 위의 내용에 의하여 영향을 받지 않습니다.

이것은 [이용허락규약\(Legal Code\)](#)을 이해하기 쉽게 요약한 것입니다.

[Disclaimer](#)

이학석사학위논문

**Lattice preferred orientation (LPO) of olivine,
amphibole, and chlorite found in hydrated mantle
peridotites from Bjørkedalen, southwestern
Norway and implications for seismic anisotropy**

노르웨이 남서부 비에르케달렌 지역의 수화된 맨틀
감람암에서 발견된 감람석, 각섬석, 그리고 녹니석의
격자선호방향과 지진파 비등방성

2015년 8월

서울대학교 대학원

지구환경과학부

강현선

Abstract

Understanding lattice preferred orientations (LPOs) of olivine is important in the study of mantle flow and seismic anisotropy of the upper mantle of the Earth. Hydrous phases such as amphibole and chlorite, on the other hand, are elastically very anisotropic compared to olivine. Even though olivine is the major mineral that constitutes the upper mantle of the Earth, both amphibole and chlorite in a deformed peridotite under water-rich condition may develop LPO that can significantly affect the seismic anisotropy. Therefore, LPOs of olivine, amphibole, and chlorite in amphibole peridotites from Bjørkedalen, southwestern Norway were studied using SEM/EBSD (Electron Backscattered Diffraction) technique. Seismic velocity and seismic anisotropy were calculated using LPOs of studied minerals.

In this study, a gradual change in olivine LPO was observed. One sample showed that [100] axes are aligned subparallel to lineation and [010] axes subnormal to foliation, which is known as type-A LPO. The other sample showed that [010] axes are aligned subnormal to foliation and [001] axes parallel to lineation, which is known as type-B LPO. Other samples showed intermediate type between type-A and type-B LPO. Amphibole LPOs showed that [001] axes are aligned subparallel to lineation and [100] axes

subnormal to foliation. Chlorite LPOs showed that [100] axes are aligned subparallel to lineation and [001] axes subnormal to foliation. The P- and S-wave anisotropies of amphibole were up to 15.2% and 11.9%, respectively, while those of chlorite were up to 25.2% and 46.2%, respectively. It turned out that seismic anisotropy of both amphibole and chlorite is much higher than that of olivine. In addition, it was found that amphibole and chlorite contribute to strong trench-parallel seismic anisotropy depending on flow geometry. This study suggests that the existence of the LPO of amphibole and chlorite in a hydrated peridotite changes the seismic anisotropy of the whole rock significantly.

Keywords

olivine, amphibole, chlorite, lattice preferred orientation, seismic anisotropy,

Bjørkedalen

Student Number: 2013-22966

Contents

Abstract	i
Contents	iii
List of tables	v
List of figure captions	vi
Chapter 1. Introduction	1
Chapter 2. Geological setting of the study area	4
Chapter 3. Sample description	7
Chapter 4. Methods	9
4.1. Measurement of LPOs and calculation of seismic anisotropy.....	9
4.2. Observation of dislocation microstructures.....	10
4.3. Identification of hydrous inclusions in olivine and orthopyroxene	11
4.4. Identification of inclusions in olivine.....	12
4.5. Mineral compositions and temperature estimation...	12
Chapter 5. Results	14
5.1. Microstructure.....	14
5.2. Mineral chemistry	14
5.3. Temperature-pressure-stress estimation.....	15

5.4. LPO of minerals.....	16
5.5. Seismic velocity and anisotropy	17
5.6. Dislocation microstructure.....	19
5.7. FTIR study: Identification of hydrous inclusions in olivine and orthopyroxene	20
5.8. Raman study: Identification of inclusions in olivine	20
Chapter 6. Discussion.....	46
6.1. Origin of the Bjørkedalen peridotites	46
6.2. Mechanisms for fabric transition in olivine.....	46
6.3. Effect of LPO of hydrous phases on whole rock seismic anisotropy.....	48
Chapter 7. Conclusion.....	57
References	59
국문요약	71

List of tables

Table 1. Modal composition of studied peridotite samples	8
Table 2. Mineral chemistry of olivine	22
Table 3. Mineral chemistry of orthopyroxene.....	23
Table 4. Mineral chemistry of amphibole	24
Table 5. Mineral chemistry of chlorite.....	25
Table 6. Mineral chemistry of spinel.....	26
Table 7. Stress estimated from recrystallized grain size of olivine under wet and dry condition.....	27
Table 8. Fabric type and strength (M-index) of studied peridotite samples	28
Table 9. Seismic anisotropies of P- and S- waves for olivine, amphibole, chlorite, and whole rock.....	29

List of figure captions

Figure 1. Geological map of Bjørkedalen, southwestern Norway	6
Figure 2. Optical photomicrograph showing microstructure of studied peridotite samples	30
Figure 3. Pole figures of olivine.....	31
Figure 4. Pole figures of amphibole.....	32
Figure 5. Pole figures of chlorite.....	33
Figure 6. Seismic anisotropy of olivine	34
Figure 7. Seismic anisotropy of amphibole.....	35
Figure 8. Seismic anisotropy of chlorite	36
Figure 9. Seismic anisotropy of whole rock.....	37
Figure 10. The relationship between relative hydrous mineral content (%) and seismic anisotropy (%) considering LPOs of olivine, amphibole, and chlorite in sample 1194-2	38
Figure 11. Effect of dip angle (θ) from $\theta=0^\circ$ to $\theta=60^\circ$ on the seismic anisotropy of olivine considering the LPO of	

olivine in sample 1194-2.....	39
Figure 12. Effect of dip angle (θ) from $\theta=0^\circ$ to $\theta=60^\circ$ on the seismic anisotropy of amphibole considering the LPO of amphibole in sample 1194-2.....	40
Figure 13. Effect of dip angle (θ) from $\theta=0^\circ$ to $\theta=60^\circ$ on the seismic anisotropy of chlorite considering the LPO of chlorite in sample 1194-2.....	41
Figure 14. Effect of dip angle (θ) from $\theta=0^\circ$ to $\theta=60^\circ$ on the seismic anisotropy of whole rock considering the modal proportion and LPOs of olivine, amphibole, and chlorite in sample 1194-2.....	42
Figure 15. Dislocation microstructures of olivine in sample 1196-3 (type-A+B LPO) and 1194-2 (type-B LPO).....	43
Figure 16. FTIR spectra of olivine and orthopyroxene in samples 1196-3 (type-A+B LPO) and 1194-2 (type-B LPO).....	44
Figure 17. Representative Raman spectra of host mineral (olivine) and inclusions of samples showing both type-A+B LPO (1196-3) and type-B LPO (1194-2).....	45
Figure 18. Olivine–spinel mantle array (OSMA) trend (Arai, 1994) showing cratonic origin of the Bjørkedalen peridotites.....	54

Figure 19. Effect of dip angle (θ) on the seismic anisotropy of olivine, amphibole, chlorite, and whole rock considering the LPOs of the three minerals within sample 1194-2....55

Chapter 1. Introduction

Subduction zones are unique places where hydrous phases transport water into the deep Earth. Subducting hydrous slab releases water into the overlying mantle wedge on its dehydration reaction as it goes deeper to higher pressure environment. Mantle hydration includes both hydrogen incorporation in nominally anhydrous phases (e.g. olivine and pyroxenes) and formation of hydrous phases such as serpentine, talc, amphibole, chlorite, brucite, and clinohumite. Shear localization in mantle results in strong lattice preferred orientation (LPO) of the constituent minerals and cause anisotropic seismic properties. In this regard, knowledge of the LPO and anisotropic seismic properties of those minerals is important in that it enables us to deduce the mantle flow patterns.

Water content of olivine, the most abundant mineral of the upper mantle, is known as one of the key factors affecting olivine LPO formation (Jung and Karato, 2001a). Previous experimental studies showed that five different LPOs of olivine (type-A -B, -C, -D, and -E) are developed depending on its water content and stress conditions during deformation (Jung and Karato, 2001a; Jung et al., 2006; Karato et al., 2008; Katayama et al., 2004). Studies on natural rock samples also showed water and stress dependence of olivine fabric (Frese et al., 2003; Jung, 2009; Jung et al., 2013; Jung et al., 2009a; Katayama et al., 2005; Kim and Jung, 2015; Linckens et al., 2011; Möckel,

1969; Mehl et al., 2003; Mizukami et al., 2004; Park et al., 2014; Park and Jung, 2015; Sawaguchi, 2004; Skemer et al., 2006; Tasaka et al., 2008; Toxopeus, 1976, 1977). Type-A olivine LPO typically occurs under dry and low stress environment and is defined by [100] axes aligned subparallel to shear direction and [010] axes aligned subnormal to shear plane (Jung and Karato, 2001a). On the other hand, type-B, type-C, and type-E olivine LPOs can be developed under wet environment and are differed by stress condition (Jung and Karato, 2001a; Jung et al., 2006). Type-B olivine LPO is characterized by its [001] axes aligned subparallel to shear direction and [010] axes aligned subnormal to shear plane. Type-C olivine LPO has its [001] axes aligned subparallel to shear direction and [100] axes subnormal to shear plane. Type-E olivine LPO is defined by its [100] axes aligned subparallel to shear direction and [001] axes subnormal to shear plane. Type-D is defined by olivine [100] axes aligned parallel to shear direction and both [010] and [001] axes aligned forming a girdle shape subnormal to shear direction.

The hydrous phases are known as elastically very anisotropic. Recently few studies on LPOs of serpentine, talc, amphibole, chlorite, brucite and clinohumite showed their contribution in anisotropic seismic properties in subduction zones (Hirauchi et al., 2010; Jung, 2011; Katayama et al., 2009; Kim and Jung, 2015; Ko and Jung, 2015; Mainprice and Ildefonse, 2009; Morales et al., 2013; Nishii et al., 2011). In this paper we present a

combined microstructural and petrologic study of the Bjørkedalen peridotite body located within the Western Gneiss Region of southwestern Norway. The Bjørkedalen peridotites provide us rare natural samples having hydrated mantle assemblage containing olivine, amphibole, and chlorite. This study investigates LPO-formation of olivine and hydrous minerals and its effect on seismic anisotropy under water-rich conditions like subduction zone. Our results suggest that water induced fabric change of olivine and the LPO of amphibole and chlorite change the seismic anisotropies of the hydrated mantle wedge.

Chapter 2. Geological setting of the study area

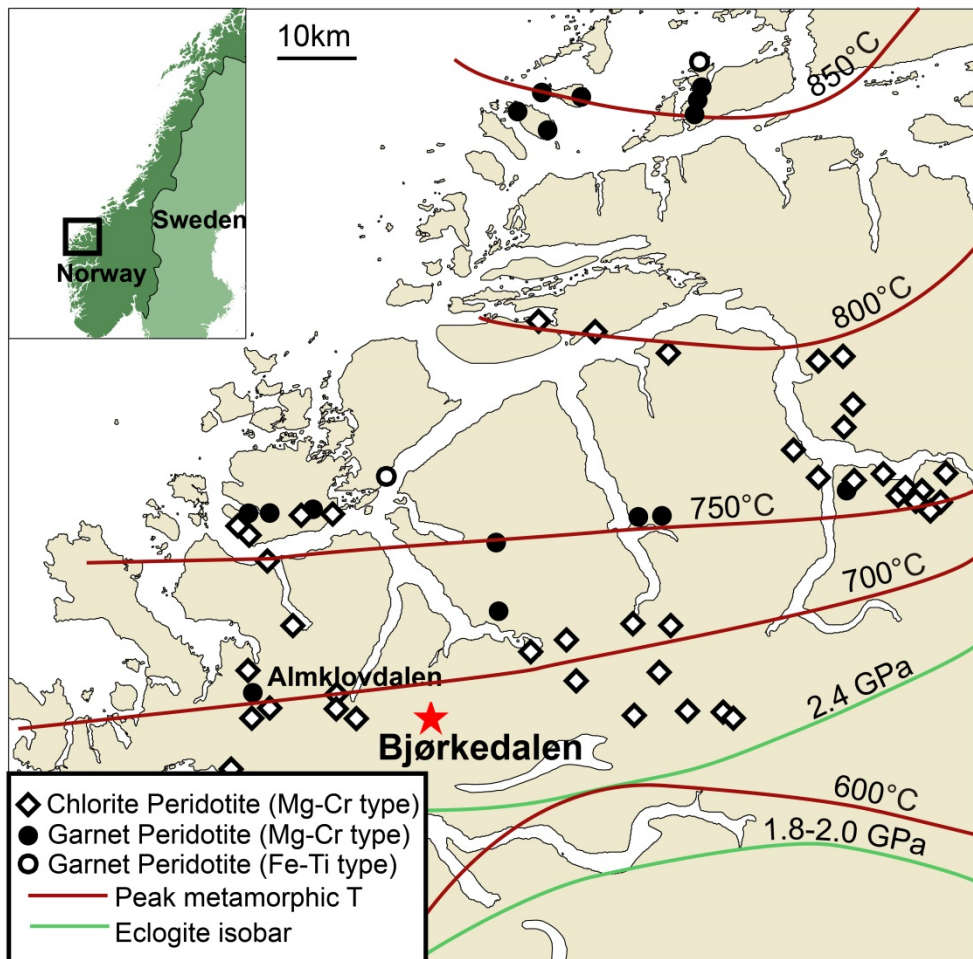
The Western Gneiss Region (WGR) of Norway is an elongate area that extends 300 km in length and 150 km in width between Bergen and Trondheim (Beyer, 2006; Cuthbert et al., 2000). The WGR is the lowest exposed tectonic unit of the Scandinavian Caledonides, a mountain system composed of nappe units that are juxtaposed by collision between Baltica and Laurentia during Scandian Orogeny (420–380 Ma) (Brueckner and Van Roermund, 2004; Roberts, 2003; Roberts and Gee, 1985; Spengler et al., 2009; Stephens and Gee, 1989). The continental collision resulted in high to ultrahigh-pressure metamorphism over the WGR, which is interpreted as a western margin of the Baltica that subducted under the Laurentian lithospheric mantle (Cuthbert et al., 2000; Krogh, 1977; Kylander-Clark et al., 2007; Root et al., 2005). The WGR consists of various rock types, mostly amphibolite- to granulite-facies gneiss, eclogites, and pods and lenses of orogenic peridotites (Hacker et al., 2010; Lapen et al., 2009).

The peridotites in the WGR are known as fragments of Archean mantle that are enclosed within the Proterozoic Baltic continental crust during subduction of Baltica underneath Laurentia (Beyer et al., 2012). The peridotites typically contain garnet or spinel bearing assemblages that have undergone various degrees of retrogression. Garnet-bearing peridotites show

evidence of refertilization during Proterozoic melt percolation event, while some of the garnet-free peridotites have extremely depleted composition formed by melt extraction during Archean (Beyer, 2006; Griffin et al., 2009).

Bjørkedalen of the central-western part of the WGR is the place where the peridotites rich in amphibole and chlorite are distributed (Fig. 1). They are metamorphosed under amphibolite facies condition and are associated with extensive hydration. The hydrous minerals amphibole and chlorite in the peridotites are interpreted as a result of interaction between peridotites and hydrated crusts during Caledonian orogeny (Carswell, 1986). The phengite dehydration reaction in the surrounding gneisses of the Baltic crust may have provided water to hydrate peridotite during exhumation and decompression process (Brueckner et al., 2010).

Figure 1. Geological map of Bjørkedalen, southwestern Norway. The study area is marked as a red star. The distribution of chlorite and garnet peridotite bodies are modified after (Lapen et al., 2009), eclogite isobar is after (Hacker et al., 2010), and the peak metamorphic temperature is after (Kylander-Clark et al., 2008).



Chapter 3. Sample description

Four peridotites (1190, 1193, 1196, and 1194) from Bjørkedalen were selected for study. The studied samples are fine-grained and well-foliated dunites with a porphyroclastic texture (Fig. 2a). They are mostly composed of olivine (59–99%), amphibole (0–41%), and chlorite (0.2–10%) and a minor orthopyroxene and spinel. The modal compositions of studied samples are shown in Table 1. The sample 1190 is characterized by high content of olivine (99%) and rare grains of orthopyroxene, chlorite, and chromite. The sample 1193 also has high olivine content (98%) but has amphibole, chlorite, and chromite. The sample 1196 is characterized by heterogeneous distribution of amphibole and chlorite. On the basis of their content, we subdivided the sample into three different parts: 1196-1, 1196-2, and 1196-3. The sample 1196-1 contains 11% amphibole and 4% chlorite. The sample 1196-2 hosts the most abundant amphibole content (41%) among the analyzed samples and rare chlorite (0.2%). The sample 1196-3 has 10% amphibole and 9% chlorite. The sample 1194 is characterized by heterogeneous distribution of chlorite, and also is subdivided into two different parts: 1194-1 and 1194-2. While both samples have similar proportion of amphibole (~10%), the sample 1194-2 contains the most abundant chlorite content (10%) among the analyzed samples.

Table 1. Modal composition of studied peridotite samples.

Sample	Modal composition (%)				
	Ol	Amp	Chl	Opx	Spl
1190	99.4	0.0	0.2	0.3	0.1
1193	97.7	0.1	1.0	1.0	0.2
1196-1	79.8	11.0	4.0	4.7	0.6
1196-2	58.5	40.8	0.2	0.0	0.5
1196-3	76.9	9.5	9.3	3.7	0.6
1194-1	87.5	10.4	2.0	0.0	0.1
1194-2	77.5	10.2	9.9	2.1	0.3

Ol: olivine, Amp: amphibole, Chl: chlorite, Opx: orthopyroxene, and Spl: spinel.

Chapter 4. Methods

4.1. Measurement of LPOs and calculation of seismic anisotropy

The foliation of the Bjørkedalen dunites were determined by well-developed schistosity made of parallel alignment of flattened olivine, flakes of chlorite and amphibole. The lineation was determined by measuring the shape preferred orientation of olivine and orthopyroxene on foliation plane, using the projection-function method (Panozzo, 1984). Next, thin sections on X-Z plane were prepared (X: lineation, Z: normal to foliation) and were coated with carbon to prevent charging in the scanning electron microscope (SEM) operation. LPOs of minerals were measured using Electron backscattered diffraction (EBSD) system attached to SEM, JEOL JSM-6380 at the School of Earth and Environmental Sciences (SEES) in Seoul National University (SNU), Korea. The Kikuchi band patterns for individual grains were manually indexed with Oxford Channel 5 software. The EBSD analysis was conducted under conditions of 15kV accelerating voltage, 60 spot size, and 15 mm working distance on samples tilted 70°. M-index was calculated to compare fabric strength of LPOs of each mineral (Skemer et

al., 2005). It is defined as $M \equiv \frac{1}{2} \int |R^T(\theta) - R^0(\theta)| d\theta$, where $R^T(\theta)$ denotes theoretical distribution of misorientation angles with random fabric and $R^0(\theta)$ denotes distribution of observed misorientation angles.

Seismic velocity and anisotropy of P- and S- wave were calculated with a FORTRAN program provided by Mainprice (1990), using measured LPOs, density, and elastic constants of olivine (Abramson et al., 1997), amphibole (Aleksandrov and Ryzhova, 1961), and chlorite (Aleksandrov and Ryzhova, 1961). P-wave velocity anisotropy (AVp) was calculated as $[(V_{p_{\max}} - V_{p_{\min}}) / ((V_{p_{\max}} + V_{p_{\min}}) * 0.5)] * 100$. S-wave velocity anisotropy (AVs) was calculated as $[(V_{s1} - V_{s2}) / ((V_{s1} + V_{s2}) * 0.5)] * 100$, where V_{s1} represents the fast S-wave velocity and V_{s2} the slow one.

4.2. Observation of dislocation microstructures

The dislocation microstructures of olivine were observed using an SEM, JEOL JSM-6380 at the SEES, SNU. Oxygen decoration technique (Jung and Karato, 2001a; Karato, 1987; Kohlstedt et al., 1976) was applied to observe dislocations in olivine. In this method, samples (1196-3 and 1194-2) were made into chips and were heated in air for 1 hour at 800°C for oxidization. A thin oxide layer produced by heating on the sample surface was removed by SYTON (colloidal silica) polishing. Then the samples were carbon-

coated to obtain clear backscattered electron (BSE) images. The SEM working conditions were as follows: 15 kV acceleration voltage, 10 mm working distance, and 60 spot size.

4.3. Identification of hydrous inclusions in olivine and orthopyroxene

The hydrous inclusions hosted in olivine and orthopyroxene in specimens 1196-3 and 1194-2 were identified using Fourier transformation infrared (FTIR) spectroscopy. The two samples (1196-3 and 1194-2) were polished on both sides to make slices with thickness of 90 ± 15 μm and 100 ± 15 μm , respectively. Polished samples were soaked in acetone for 24 hours to eliminate adhesives, and were heated at 120°C for 24 hours afterwards to get rid of water existing on the surface or along the grain boundary. The unpolarized FTIR absorption spectra were obtained at room temperature and pressure with a Nicolet 6700 Fourier transform infrared (FTIR) spectrometer equipped with a continuum IR microscope housed at Tectonophysics laboratory, SNU, Korea. It used an unpolarized light source with a KBr beam splitter and an MCT detector. Moisture in air was removed by N_2 purging on the sample chamber. The aperture size was set to 50×50 μm . Each FTIR spectrum was averaged in a series of 128 scans to reduce noises and has a resolution of 4 cm^{-1} .

4.4. Identification of inclusions in olivine

Micrometer to submicrometer scale inclusions within olivine hosts were identified with Raman spectroscopy. A confocal dispersive DXR Raman microscope housed at Tectonophysics laboratory in SNU, Korea was used for the identification. The Raman microscope is equipped with an Ar laser with 532 nm wavelength and 10 mW power. The 50× objective lens and 0.7 μm laser size was applied in this analysis to make sure small inclusions to be identified. For each Raman spectrum, sample was exposed 64 times to reduce noises on the resulting spectrum. Samples were photobleached for 1 min and fluorescence correction with 6th order polynomial was applied to reduce excitation of baseline due to the fluorescent material such as glass sample holder.

4.5. Mineral compositions and temperature estimation

Mineral compositions of Bjørkedalen peridotites were analyzed with electron probe micro-analyzer (EPMA) SHIMADZU 1600 at Korea Basic Science Institute (KBSI) Jeonju Center. Major constituent elements of olivine, orthopyroxene, amphibole, chlorite, and spinel were quantitatively analyzed as oxide weight percentages. The EPMA was operated under 15 kV accelerating voltage, 20 nA beam current, and 1 μm beam size

conditions. The results were processed with Minpet 2.02 to give chemical formula of given minerals.

Chapter 5. Results

5.1. Microstructure

Peridotites from Bjørkedalen contain porphyroclasts of olivine and orthopyroxene enclosed in a fine-grained matrix of olivine and orthopyroxene (Fig. 2a). Recrystallization was intense in all of the studied samples (Fig. 2b). The size of olivine and orthopyroxene porphyroclasts ranges up to 5000 μm while that of recrystallized olivine and orthopyroxene in matrix is 100–200 μm . Some olivine porphyroclasts are very strained and show undulose extinction (Fig. 2c). Subgrain boundaries are well developed in olivine porphyroclasts. Recrystallized olivines are anhedral and their grain shape is slightly elongated as a consequence of the deformation process. Amphibole occurs as column or needle shaped crystals with relatively large grain size (up to 2000 μm) (Fig. 2e). Chlorite occurs as discrete flakes or ribbons and is associated with disseminated fine grained chromite (Figs. 2d and 2f). Amphibole and chlorite are aligned subparallel to lineation defined by elongated olivine (Figs. 2e and 2f).

5.2. Mineral chemistry

Representative compositions of the minerals comprising the Bjørkedalen

peridotites are summarized in Tables 2–6. Both olivine and orthopyroxene show depleted composition. Olivine belongs to forsterite with high Mg# (92.4–93.1) and is homogeneous without zoning. Orthopyroxene is classified as enstatite. Their composition is highly magnesian with Mg# 92.3–93.2 and is very low in Al₂O₃ contents (0.05–0.12 wt.%). Two different varieties of amphibole are identified in Bjørkedalen peridotites. One rich in CaO contents is defined as tremolite, while the other one relatively rich in MgO and FeO contents is classified as magnesio-cummingtonite. Chlorite composition varies from clinocllore to penninite. It has high MgO (34–36 wt.%) and low FeO (1–3 wt.%) content, resulting in a high Mg# (96.1–97.8). Spinel is characterized by its low Mg# (16.3–34.6) and high Cr# (84.4–90.8) and can be classified as chromite.

5.3. Temperature-pressure-stress estimation

The equilibrium temperature of the Bjørkedalen peridotites was calculated using an empirical geothermometer based on the solubility of Cr and Al in orthopyroxene within spinel peridotite (Witt-Eickschen and Seck, 1991). The estimated equilibrium temperature of the samples ranges from 650 to 700°C. Equilibrium pressure of the specimens should be under 2 GPa considering the stable pressure conditions of spinel. The differential stress of a sample was estimated from recrystallized grain size of olivine under

wet and dry condition (Jung and Karato, 2001a). Two-dimensional (2-D) recrystallized olivine grain size was calculated using linear intercept method, and three-dimensional (3-D) size was given by multiplying the 2-D size by 1.5 (Gifkins, 1970). Recrystallized grain size of olivine ranges from 101 to 134 μm (Table 7) and indicates that the studied peridotites underwent stress of 37 ± 15 MPa in dry condition or 87 ± 15 MPa in wet condition.

5.4. LPO of minerals

In this study, olivine showed type-A LPO, type-B LPO, and a mixed LPO between type-A and type-B (Fig. 3). Types of olivine LPO and fabric strength for each sample are summarized in Table 8. One sample (1190) showed that [100] axes are aligned subparallel to lineation and [010] axes subnormal to foliation, which is known as type-A LPO. The other two samples (1194-1 and 1194-2) showed that [010] axes are aligned subnormal to foliation and [001] axes parallel to lineation, which is known as type-B LPO (Jung and Karato, 2001a). Other samples (1193, 1196-1, 1196-2, and 1196-3) showed intermediate type between type-A and type-B LPO (type-A+B LPO).

LPO of amphibole in five samples showed that [001] axes are aligned subparallel to lineation and [100] axes subnormal to foliation (Fig. 4). This result corresponds to type-I of the amphibole LPO types suggested by recent

experimental study (Ko and Jung, 2015). All of the two chlorite LPOs showed that [100] axes are aligned subparallel to lineation and [001] axes subnormal to foliation (Fig. 5). Chlorite LPOs have not been defined by systematic experimental study. However, LPOs of naturally occurring chlorites were reported by Kim and Jung (2015). The data reported in this study corresponds well with one of the types reported by the previous study.

5.5. Seismic velocity and anisotropy

The seismic velocity and anisotropy of P- and S-waves calculated for olivine, amphibole, chlorite, and whole rock are shown in Figs. 6–9. Seismic anisotropies of P- and S-waves (%) are summarized in Table 9. The olivine-rich sample (1190) with 99% olivine showed P-wave velocity anisotropy of 7.5% and maximum S-wave velocity anisotropy of 5.2%. For the chlorite-rich sample (1194-2) which consists of 78% olivine, 10% amphibole, and 10% chlorite, the P-wave velocity anisotropy of olivine, amphibole, and chlorite were 1.8%, 14.0%, and 25.2%, respectively. The P-wave velocity anisotropy of the whole rock calculated in relation to the modal ratio of those three minerals was 6.0%. The maximum S-wave velocity anisotropy of olivine, amphibole, and chlorite were calculated as 1.1%, 9.5%, and 46.2%, respectively. The maximum S-wave velocity anisotropy of the whole rock was 8.3%. For the amphibole-rich sample

(1196-2) which is composed of 59% olivine and 41% amphibole, the P-wave velocity anisotropy of olivine and amphibole were 5.5% and 15.2%, respectively. The P-wave velocity anisotropy for the whole rock (amphibole-rich) calculated with the modal ratio of the two minerals was high (9.0%). The maximum S-wave velocity anisotropy of olivine and amphibole were 4.4% and 11.9%, respectively. The maximum S-wave velocity anisotropy of the whole rock was 6.3%.

The variation of P- and S-wave anisotropy in relation with modal content of both amphibole and chlorite on olivine (1194-2) is shown in Fig. 10. A positive linear relationship existed between modal proportions of the two minerals and both P- and S- wave anisotropy. Amphibole had relatively higher values of AV_p compared with maximum AVs while chlorite showed higher maximum AVs than AV_p. The gap between AV_p and maximum AVs increased as the content of those two minerals incremented.

The effect of dipping angle of flow on the polarization direction of the fast S-wave (Vs1) was calculated using LPOs of olivine, amphibole, and chlorite in sample 1194-2 (Figs. 11-14). When the dipping angle of the subducting slab changed from 0° to 60°, the Vs1 polarization direction of the vertically propagating S-wave changed from trench-normal (x) to trench-parallel (y) direction in all the three minerals. However, the critical dip angle of change was different for each mineral. Olivine showed little variation in Vs1 polarization direction of vertically propagating S- waves when the dipping

angle of flow changed from $\theta=45^\circ$ to $\theta=60^\circ$, showing consistent oblique Vs1 polarization direction tilted 45° to the trench (Fig. 11). For amphibole, the Vs1 polarization direction of the vertically propagating S-waves changed to trench-parallel direction at the angle $\theta=45^\circ$ (Fig. 12). On the other hand, that of chlorite changed to trench-parallel direction at steeper dipping flow angle ($\theta=50^\circ$) than that of amphibole (Fig. 13). Considering the modal proportion of the three minerals, the change in Vs1 polarization direction of the whole rock was calculated in Fig. 14. The result showed a mixture of trench-normal and trench-parallel Vs1 polarization direction of the vertically propagating S-waves until the dipping angle of flow reached $\theta=50^\circ$. When the dipping angle changed to $\theta=60^\circ$ the Vs1 polarization direction changed to trench-parallel direction. The amplitude of the AVs for the vertically propagating S-waves changed from small (red colored) to large (blue colored) value with increasing dipping angle of flow except for the calculation conducted on olivine.

5.6. Dislocation microstructure

Dislocation microstructures of olivine in sample 1196-3 (type-A+B LPO) and sample 1194-2 (type-B LPO) were observed through BSE images shown in Fig. 15. Dislocations appear as bright dots and straight or curved lines in the images. Curved and straight dislocations were observed in

sample 1196-3 (Fig. 15a) while straight dislocations were generally observed in the sample 1194-2 (Fig. 15b). In both samples, dislocations are distributed heterogeneously among grains, as well as in a single grain. It is observed that dislocations align in a line to form subgrain boundaries.

5.7. FTIR study: Identification of hydrous inclusions in olivine and orthopyroxene

FTIR analysis was conducted on samples with type-A+B (1196-3) and type-B (1194-2) LPO of olivine. Hydrous inclusions were identified within olivine and orthopyroxene hosts by their distinguishable OH absorption peak positions. Representative IR spectra are shown in Fig. 16. IR absorption bands are located at wavenumbers 3690, 3689, 3688, 3687, 3685, 3684, 3682, 3677, 3673, 3662, and 3661 cm^{-1} . Peaks at 3690, 3689, 3688, 3687, 3685, and 3684 cm^{-1} are indicative of intrinsic hydroxide ($-\text{OH}$) in serpentine (Jung et al., 2013; Jung et al., 2014), while peaks at 3677, 3673, 3662, and 3661 cm^{-1} indicate existence of amphibole or talc (Miller et al., 1987; Skogby and Rossman, 1991).

5.8. Raman study: Identification of inclusions in olivine

Raman analysis on samples 1196-3 (type-A+B LPO) and 1194-2 (type-B

LPO) showed that there are inclusions such as antigorite, anthophyllite, talc, and magnesite existing within olivine hosts. Representative Raman spectra is shown in Fig. 17. Characteristic Raman spectra of antigorite corresponds to at 688 (686 and 681), 384 (381), 230 (229), and 200 (199) cm^{-1} (Figs. 17a, 17b, and 17d). Talc peaks are positioned at 1051 (1049), 676 (673), 362 (359), 194 (191), and 111 (108) cm^{-1} (Figs. 17b and 17c). Anthophyllite was identified by spectra at 678 (676), 436, and 194 cm^{-1} (Figs. 17a and 17c). The peaks at 1095, 741, 327, and 212 cm^{-1} indicate presence of magnesite.

Table 2. Mineral chemistry of olivine.

Sample	1190	1193	1196-1	1196-2	1194-1	1194-2
Mineral	Ol	Ol	Ol	Ol	Ol	Ol
SiO ₂	41.78	41.12	41.30	41.01	41.25	41.28
TiO ₂	0.00	0.01	0.01	0.01	0.00	0.00
Al ₂ O ₃	0.00	0.00	0.00	0.00	0.00	0.00
FeO	6.78	7.54	7.24	7.06	7.37	7.21
NiO	0.38	0.35	0.39	0.32	0.31	0.41
MnO	0.10	0.11	0.11	0.10	0.14	0.12
MgO	51.33	51.16	51.27	51.62	51.00	51.14
CaO	0.00	0.02	0.01	0.00	0.00	0.00
Na ₂ O	0.00	0.00	0.00	0.00	0.00	0.00
K ₂ O	0.00	0.00	0.00	0.00	0.01	0.01
Total	100.38	100.30	100.33	100.13	100.09	100.20
Numbers of ions on the basis of 4 O						
Si	1.006	0.996	0.998	0.993	1.000	0.999
Ti	0.000	0.000	0.000	0.000	0.000	0.000
Al	0.000	0.000	0.000	0.000	0.000	0.000
Fe ²⁺	0.137	0.153	0.146	0.143	0.149	0.146
Ni	0.007	0.007	0.008	0.006	0.006	0.008
Mn	0.002	0.002	0.002	0.002	0.003	0.002
Mg	1.842	1.847	1.847	1.863	1.842	1.845
Ca	0.000	0.000	0.000	0.000	0.000	0.000
Na	0.000	0.000	0.000	0.000	0.000	0.000
K	0.000	0.000	0.000	0.000	0.000	0.000
Cations	2.99	3.01	3.00	3.01	3.00	3.00
Mg#	93.08	92.35	92.67	92.87	92.52	92.67

Ol: olivine.

Table 3. Mineral chemistry of orthopyroxene.

Sample	1190	1193	1196-1	1196-2	1194-2
Mineral	Opx	Opx	Opx	Opx	Opx
SiO ₂	58.60	57.83	57.69	56.68	58.64
TiO ₂	0.00	0.01	0.02	0.01	0.03
Al ₂ O ₃	0.12	0.05	0.07	0.09	0.08
Cr ₂ O ₃	0.05	0.04	0.06	0.08	0.03
FeO	4.72	5.27	5.33	5.22	5.36
NiO	0.10	0.05	0.04	0.06	0.02
MnO	0.13	0.15	0.16	0.16	0.14
MgO	36.17	36.43	36.45	36.76	35.88
CaO	0.06	0.06	0.06	0.06	0.07
Na ₂ O	0.00	0.00	0.00	0.00	0.00
K ₂ O	0.00	0.00	0.00	0.00	0.01
Total	99.95	99.89	99.87	99.12	100.25
Numbers of ions on the basis of 6 O					
Si	2.005	1.979	1.975	1.950	2.005
Ti	0.000	0.000	0.000	0.000	0.001
Al	0.005	0.002	0.003	0.004	0.003
Cr	0.001	0.001	0.002	0.002	0.001
Fe ²⁺	0.135	0.151	0.153	0.150	0.153
Ni	0.003	0.001	0.001	0.002	0.000
Mn	0.004	0.004	0.005	0.005	0.004
Mg	1.845	1.859	1.860	1.885	1.829
Ca	0.002	0.002	0.002	0.002	0.003
Na	0.000	0.000	0.000	0.000	0.000
K	0.000	0.000	0.000	0.000	0.000
Cations	4.00	4.00	4.00	4.00	4.00
Mg#	93.18	92.49	92.40	92.63	92.28
Cr#	16.67	33.33	40.00	33.33	25.00

Opx: orthopyroxene.

Table 4. Mineral chemistry of amphibole.

Sample	1193	1196-2	1194-1	1193	1196-1	1196-2	1194-1	1194-2
Mineral	Tr	Tr	Tr	Cum	Cum	Cum	Cum	Cum
SiO ₂	56.70	54.65	56.70	57.92	59.19	57.18	56.65	58.85
TiO ₂	0.04	0.01	0.03	0.01	0.00	0.00	0.00	0.00
Al ₂ O ₃	0.78	0.98	0.79	0.07	0.31	0.10	0.14	0.11
Cr ₂ O ₃	0.06	0.13	0.03	0.03	0.06	0.04	0.01	0.01
FeO	2.35	2.00	2.16	6.24	5.49	5.30	6.08	5.59
MnO	0.08	0.07	0.05	0.26	0.22	0.23	0.27	0.20
MgO	25.09	24.78	24.69	30.65	31.39	31.44	31.13	31.28
CaO	11.12	11.68	11.83	0.56	0.50	0.50	0.59	0.57
Na ₂ O	0.30	0.35	0.30	0.05	0.02	0.03	0.03	0.01
K ₂ O	0.10	0.32	0.06	0.01	0.00	0.01	0.01	0.00
Total	96.62	94.97	96.65	95.80	97.18	94.82	94.91	96.61
Numbers of ions on the basis of 23 O								
Si	7.827	7.714	7.831	7.939	7.955	7.892	7.851	7.963
Ti	0.004	0.001	0.003	0.001	0.000	0.000	0.000	0.000
Al	0.127	0.163	0.129	0.011	0.049	0.016	0.024	0.017
Cr	0.006	0.015	0.004	0.004	0.007	0.004	0.001	0.001
Fe ²⁺	0.271	0.236	0.250	0.716	0.617	0.611	0.705	0.633
Mn	0.010	0.008	0.006	0.030	0.025	0.027	0.032	0.023
Mg	5.162	5.215	5.082	6.263	6.289	6.468	6.433	6.309
Ca	1.644	1.766	1.751	0.082	0.073	0.073	0.088	0.082
Na	0.081	0.095	0.080	0.014	0.006	0.008	0.007	0.002
K	0.018	0.058	0.011	0.001	0.001	0.001	0.001	0.000
Cations	15.15	15.27	15.15	15.06	15.02	15.10	15.14	15.03
Mg#	95.01	95.67	95.31	89.74	91.07	91.37	90.12	90.88

Tr: tremolite and Cum: cummingtonite

Table 5. Mineral chemistry of chlorite.

Sample	1190	1193	1196-1	1196-2	1194-1	1194-2
Mineral	Chl	Chl	Chl	Chl	Chl	Chl
SiO ₂	33.78	31.27	31.96	29.89	30.70	32.30
TiO ₂	0.02	0.02	0.01	0.01	0.00	0.02
Al ₂ O ₃	11.92	14.05	13.97	14.89	13.82	13.83
Cr ₂ O ₃	3.07	3.24	2.80	3.11	3.26	3.04
FeO	1.44	2.27	2.52	2.41	2.30	2.17
MnO	0.00	0.03	0.00	0.03	0.00	0.06
MgO	35.46	34.41	34.70	34.22	34.73	34.14
CaO	0.03	0.02	0.01	0.01	0.03	0.01
Na ₂ O	0.00	0.00	0.00	0.00	0.00	0.00
K ₂ O	0.01	0.00	0.00	0.00	0.01	0.00
Total	85.72	85.30	85.99	84.57	84.84	85.56
Numbers of ions on the basis of 36 O						
Si	6.460	6.060	6.137	5.857	5.993	6.218
Ti	0.003	0.003	0.001	0.002	0.000	0.003
Al	2.685	3.205	3.160	3.436	3.178	3.136
Cr	0.464	0.496	0.425	0.482	0.502	0.462
Fe ²⁺	0.230	0.368	0.405	0.395	0.375	0.349
Mn	0.000	0.004	0.000	0.005	0.000	0.010
Mg	10.109	9.940	9.934	9.998	10.107	9.796
Ca	0.007	0.003	0.001	0.002	0.006	0.001
Na	0.000	0.000	0.000	0.000	0.000	0.000
K	0.001	0.000	0.000	0.000	0.001	0.000
Cations	19.96	20.08	20.06	20.18	20.16	19.98
Mg#	97.78	96.43	96.08	96.20	96.42	96.56
Cr#	14.73	13.40	11.85	12.30	13.64	12.84

Chl: chlorite.

Table 6. Mineral chemistry of spinel.

Sample	1190	1193	1196-1	1196-2	1194-1	1194-2
Mineral	Spl	Spl	Spl	Spl	Spl	Spl
SiO ₂	0.07	0.01	0.03	0.06	0.05	0.04
TiO ₂	0.09	0.27	0.16	0.14	0.20	0.14
Al ₂ O ₃	7.01	3.55	3.75	3.58	4.95	4.77
Cr ₂ O ₃	56.58	51.00	51.07	52.51	49.32	53.13
FeO	24.57	35.67	36.09	35.06	35.57	31.30
MnO	0.44	0.54	0.53	0.60	0.50	0.46
MgO	7.30	4.16	4.16	3.84	4.17	4.65
CaO	0.00	0.02	0.00	0.00	0.00	0.00
Na ₂ O	0.02	0.00	0.00	0.01	0.00	0.01
K ₂ O	0.00	0.00	0.00	0.00	0.00	0.01
Total	96.08	95.21	95.79	95.79	94.76	94.50
Numbers of ions on the basis of 4 O						
Si	0.003	0.000	0.001	0.002	0.002	0.001
Ti	0.002	0.008	0.005	0.004	0.006	0.004
Al	0.296	0.161	0.169	0.161	0.224	0.214
Cr	1.602	1.554	1.546	1.588	1.497	1.595
Fe ²⁺	0.737	1.151	1.157	1.123	1.144	0.995
Mn	0.013	0.018	0.017	0.019	0.016	0.015
Mg	0.390	0.239	0.238	0.219	0.239	0.264
Ca	0.000	0.001	0.000	0.000	0.000	0.000
Na	0.001	0.000	0.000	0.000	0.000	0.001
K	0.000	0.000	0.000	0.000	0.000	0.000
Cations	3.04	3.13	3.13	3.12	3.13	3.09
Mg#	34.61	17.19	17.06	16.32	17.28	20.97
Cr#	84.40	90.61	90.15	90.79	86.98	88.17

Spl: spinel.

Table 7. Stress estimated from recrystallized grain size of olivine under wet and dry condition.

Sample	Recrystallized grain size (μm)	Stress (MPa) ^a	Stress (MPa) ^b
1190	130	32 \pm 15	80 \pm 15
1193	101	42 \pm 15	100 \pm 15
1196-1	105	41 \pm 15	92 \pm 15
1194-1	134	31 \pm 15	74 \pm 15

^aStress was estimated under a dry condition (Jung and Karato, 2001a).

^bStress was estimated under a wet condition (Jung and Karato, 2001a).

Table 8. Fabric type and strength (M-index) of studied peridotite samples.

Sample	Fabric type		M-index		
	Ol	Amp	Ol	Amp	Chl
1190	A	–	0.088	–	–
1193	A+B	–	0.039	–	–
1196-1	A+B	I	0.032	0.114	–
1196-2	A+B	I	0.067	0.179	–
1196-3	A+B	I	0.041	0.129	0.137
1194-1	B	I	0.033	0.166	–
1194-2	B	I	0.033	0.163	0.232

Ol: olivine, Amp: amphibole, and Chl: chlorite.

Table 9. Seismic anisotropies of P- and S- waves for olivine, amphibole, chlorite, and whole rock.

Sample	Ol		Amp		Chl		Whole rock	
	AVp	Max. AVs	Vp	Max. AVs	AVp	Max. AVs	Vp	Max. AVs
1190 ^a	7.5	5.22	–	–	–	–	7.5	5.22
1193 ^a	4.4	2.98	–	–	–	–	4.4	2.98
1196-1	2.8	1.97	10.0	9.45	–	–	3.4	2.33
1196-2 ^b	5.5	4.35	15.2	11.91	–	–	9.0	6.34
1196-3	4.6	2.87	11.5	7.54	22.3	31.56	7.4	6.70
1194-1	1.9	1.14	15.0	10.47	–	–	3.3	1.93
1194-2 ^c	1.8	1.06	14.0	9.50	25.2	46.23	6.0	8.32

^aOlivine rich sample 1190 (99.5% Ol) and 1193 (97.7 % Ol).

^bAmphibole rich sample 1196-2 (40.8 % Amp).

^cChlorite rich sample 1194-2 (9.9 % Chl).

AVp: seismic anisotropy of P-wave, and Max. AVs: maximum seismic anisotropy of S-wave.

Ol: olivine, Amp: amphibole, and Chl: chlorite.

Figure 2. Optical photomicrograph showing microstructure of studied peridotite samples. (a, b) Cross-polarized light image showing Ol-rich samples (1190 and 1193). (c) Ol porphyroblast embedded within the matrix of Ol and Opx (sample 1190). (d) Plane-polarized light image showing disseminated chromites (Chr) occurring within Chl (sample 1193). (e) Elongated Ol and Amp aligned subparallel to lineation (sample 1196-2). The picture was taken with λ -plate inserted. (f) Elongated Ol and Chl aligned subparallel to lineation (sample 1194-2). The horizontal and vertical directions of all pictures are parallel to lineation and normal to foliation of the specimen, respectively. Yellow arrows indicate undulose extinction. Ol: olivine, Amp: amphibole, Opx: orthopyroxene, Chl: chlorite, and Chr: chromite.

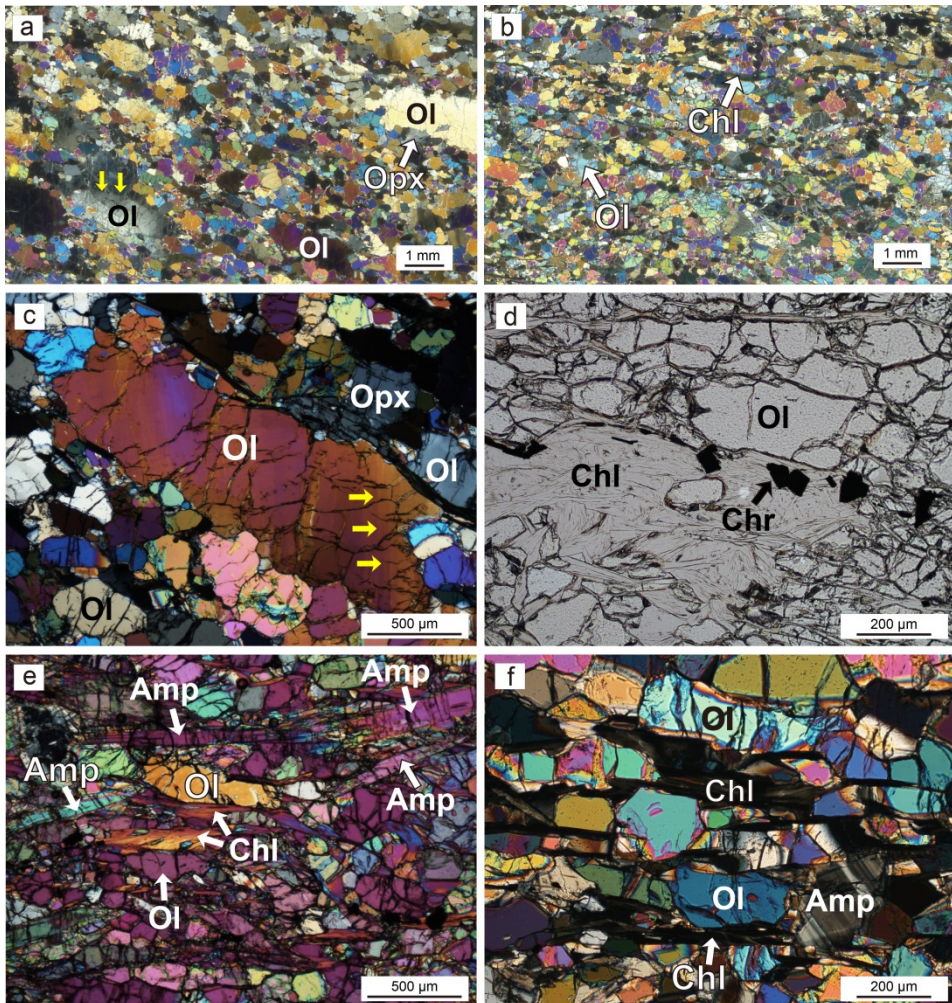


Figure 3. Pole figures of olivine. Pole figures are plotted in the lower hemisphere using an equal area projection. Foliation is indicated as white line, and lineation is indicated as red dot. A half scatter width of 20° was used. S: foliation; L: lineation; N: number of grains.

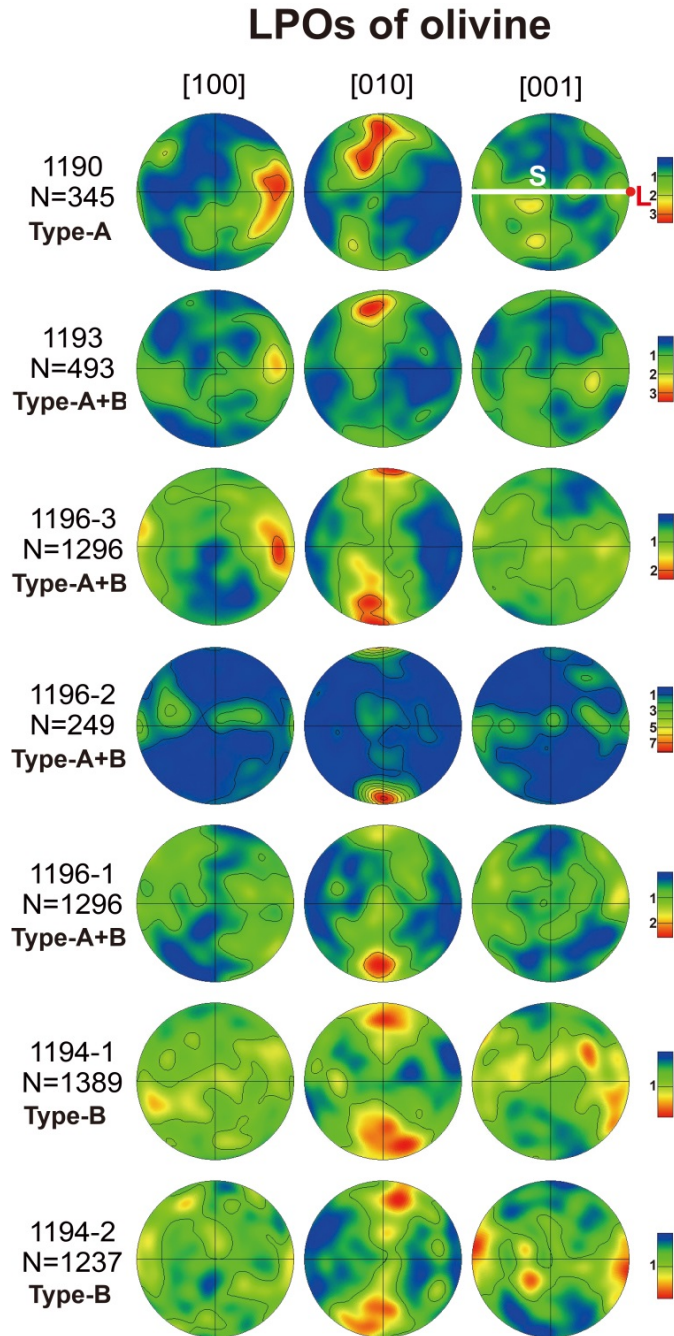


Figure 4. Pole figures of amphibole. Pole figures are plotted in the lower hemisphere using an equal area projection. Foliation is indicated as white line, and lineation is indicated as red dot. A half scatter width of 20° was used. S: foliation; L: lineation; N: number of grains.

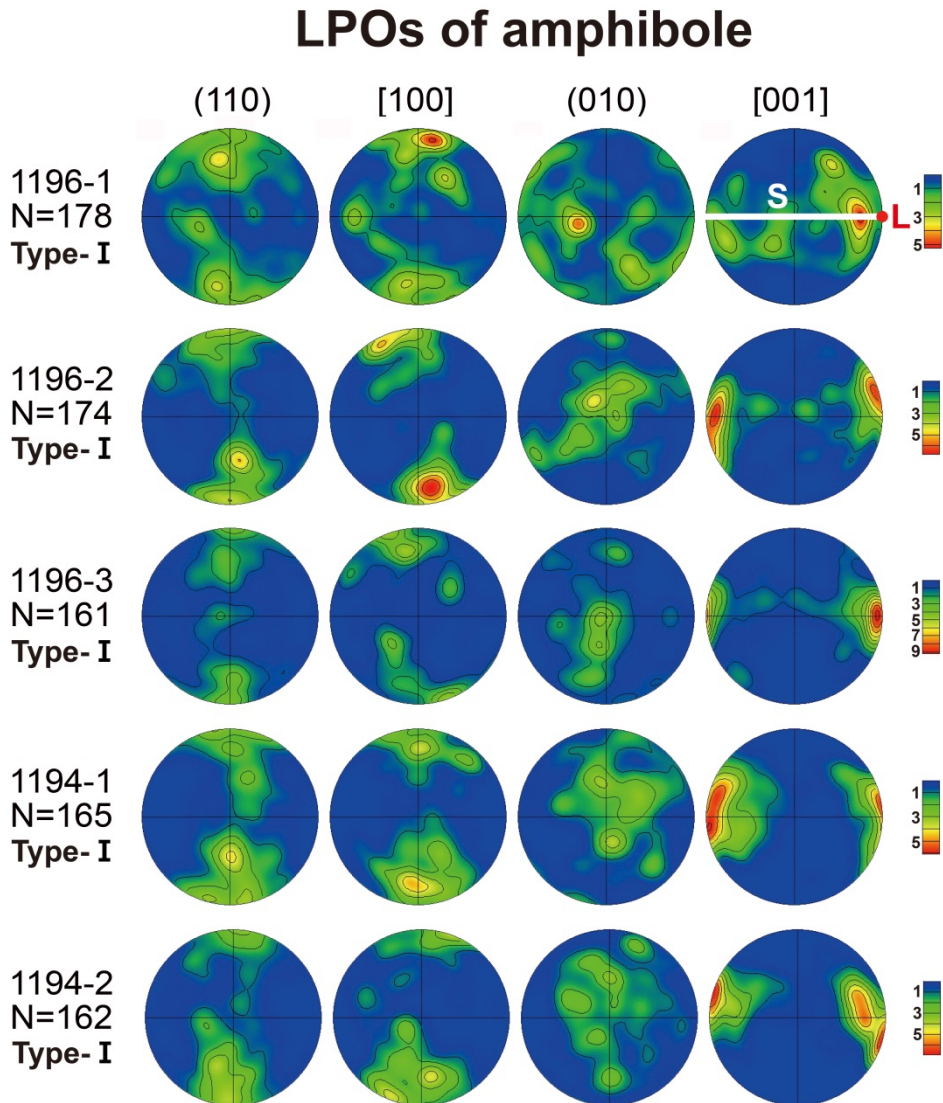


Figure 5. Pole figures of chlorite. Pole figures are plotted in the lower hemisphere using an equal area projection. Foliation is indicated as white line, and lineation is indicated as red dot. A half scatter width of 20° was used. S: foliation; L: lineation; N: number of grains.

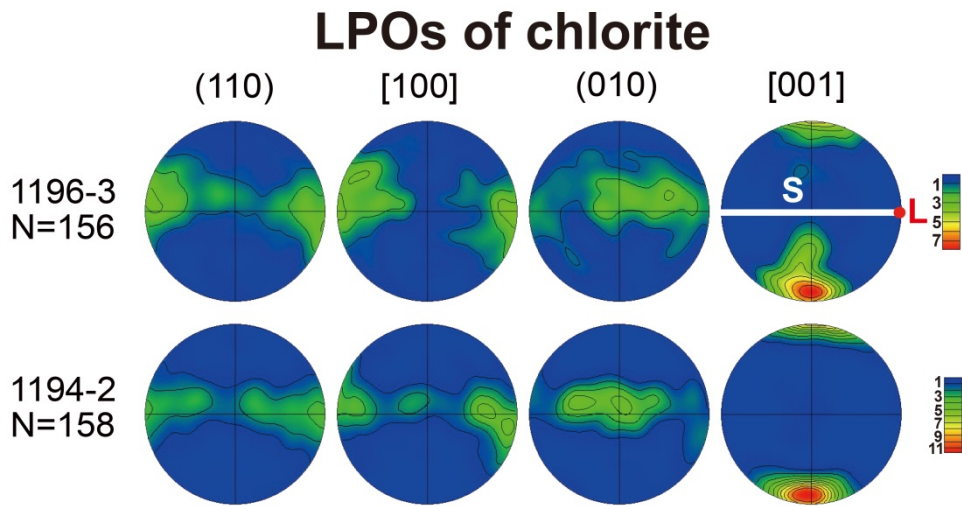


Figure 6. Seismic anisotropy of olivine. The x direction corresponds to the lineation, and the z direction of the plot is the direction normal to the foliation. P-wave velocity (V_p), S-wave anisotropy (AV_s), and polarization direction of faster shear wave ($Vs1$) are plotted.

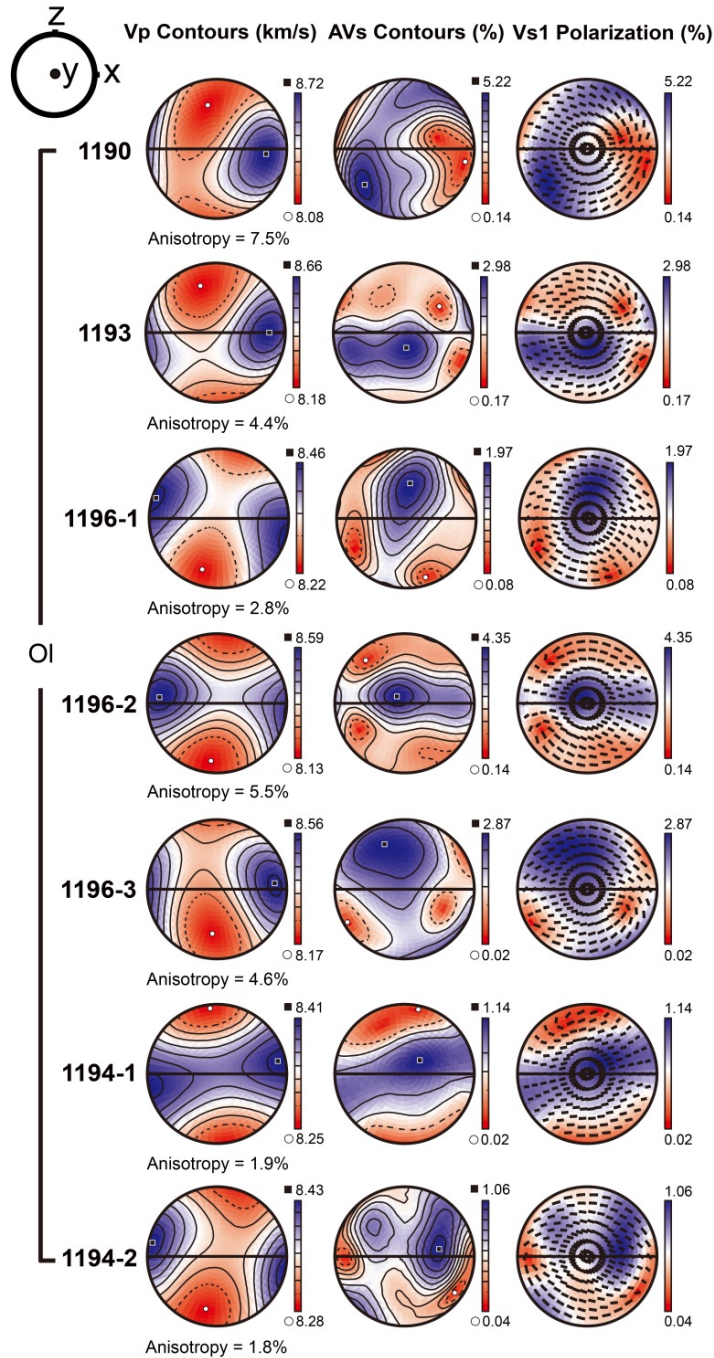


Figure 7. Seismic anisotropy of amphibole. The x direction corresponds to the lineation, and the z direction of the plot is the direction normal to the foliation. P-wave velocity (V_p), S-wave anisotropy (AVs), and polarization direction of faster shear wave (V_{s1}) are plotted.

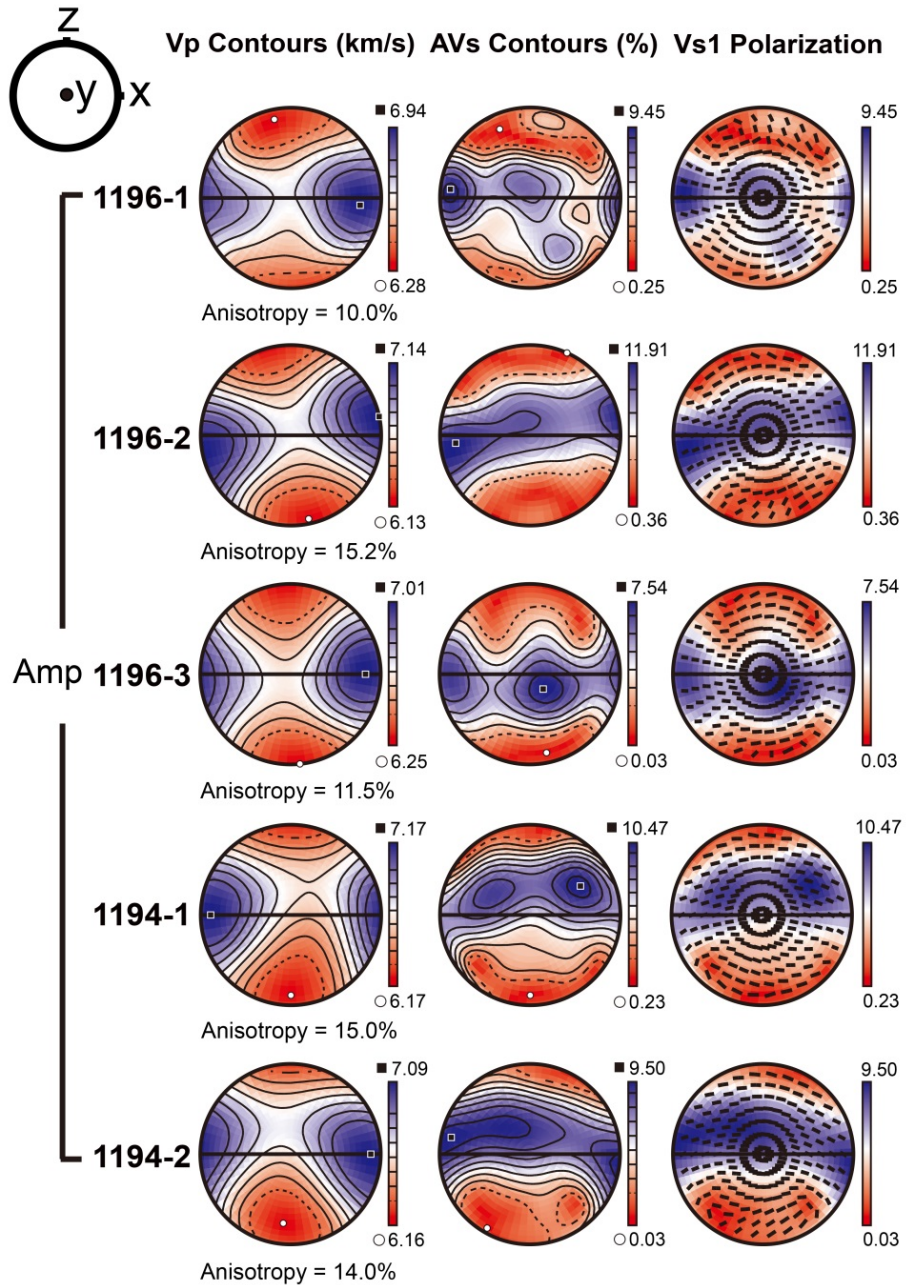


Figure 8. Seismic anisotropy of chlorite. The x direction corresponds to the lineation, and the z direction of the plot is the direction normal to the foliation. P-wave velocity (V_p), S-wave anisotropy (AVs), and polarization direction of faster shear wave (V_{s1}) are plotted.

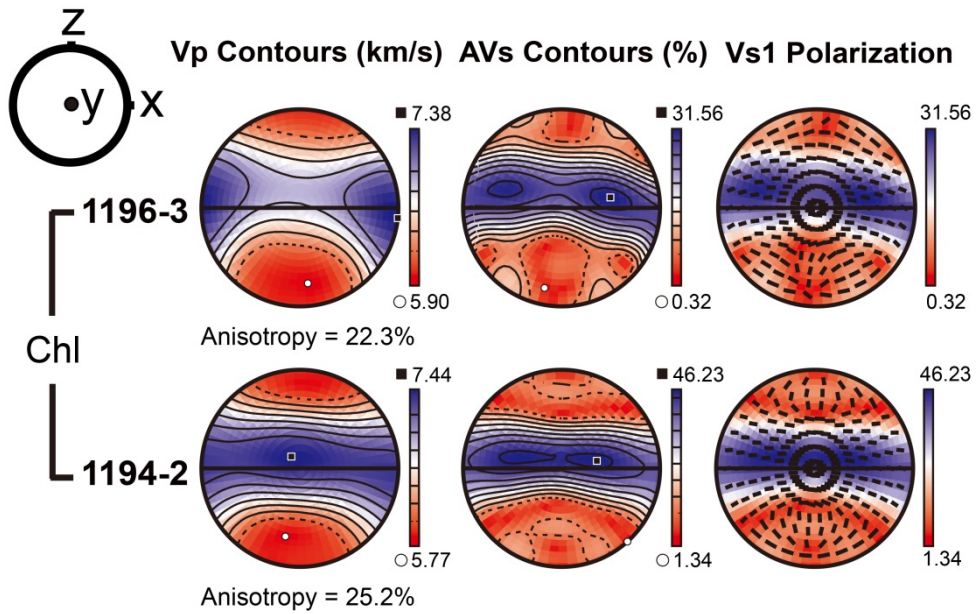


Figure 9. Seismic anisotropy of whole rock. The x direction corresponds to the lineation, and the z direction of the plot is the direction normal to the foliation. P-wave velocity (V_p), S-wave anisotropy (AVs), and polarization direction of faster shear wave (V_{s1}) are plotted.

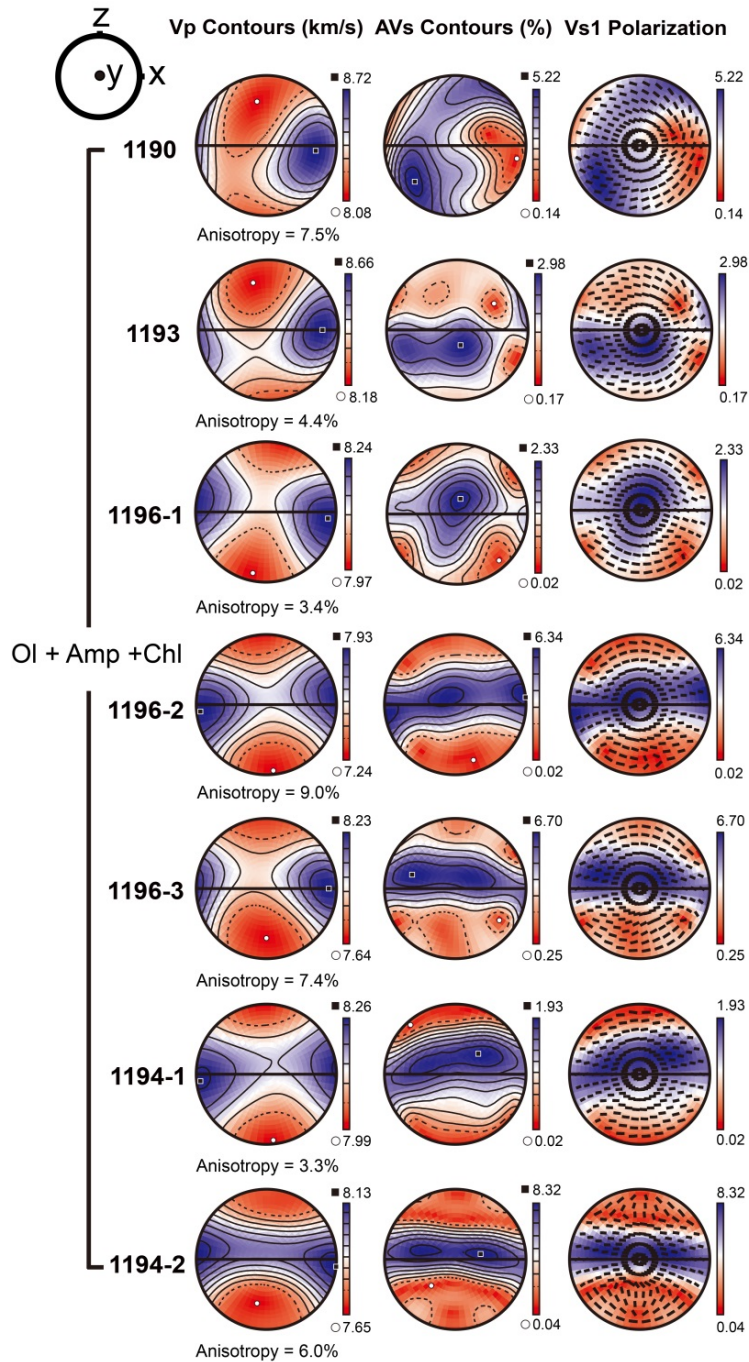
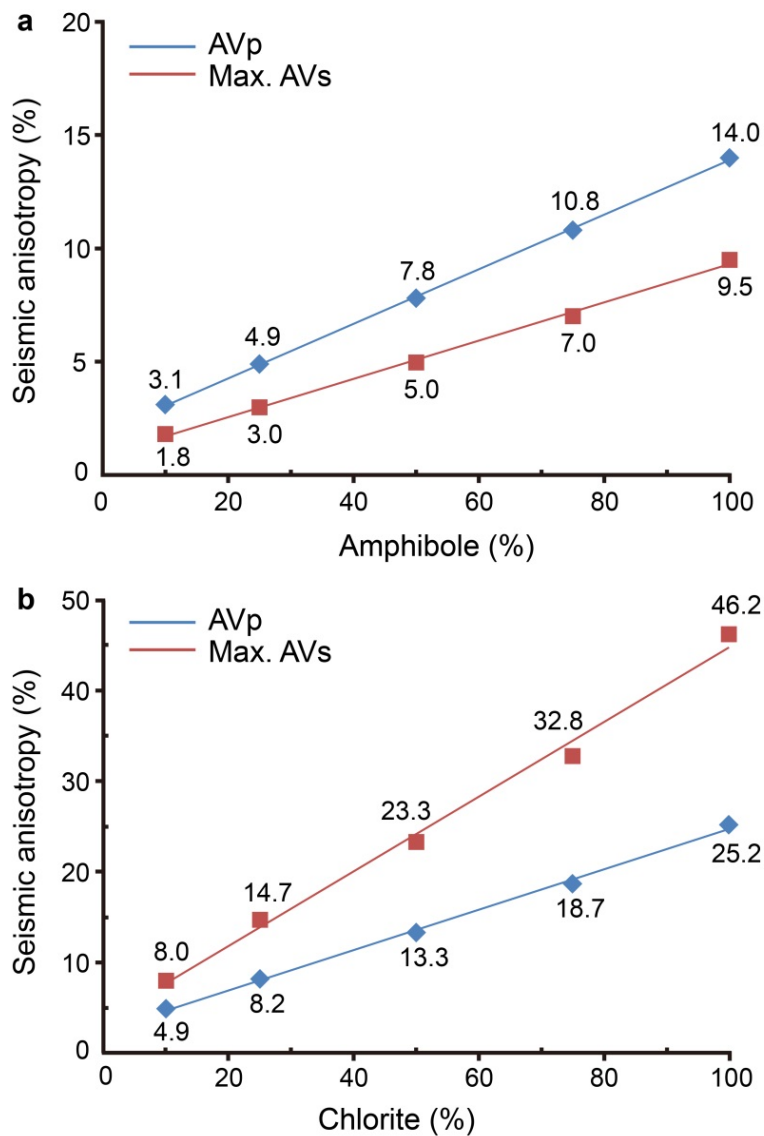


Figure 10. The relationship between relative hydrous mineral content (%) and seismic anisotropy (%) considering LPOs of olivine, amphibole, and chlorite in sample 1194-2. (a) The relationship between amphibole content (%) and seismic anisotropy (%). (b) The relationship between chlorite content (%) and seismic anisotropy (%).



AVp: P-wave anisotropy and Max. AVs: maximum S-wave anisotropy.

Figure 11. Effect of dip angle (θ) from $\theta=0^\circ$ to $\theta=60^\circ$ on the seismic anisotropy of olivine considering the LPO of olivine in sample 1194-2. P-wave velocity (V_p), S-wave anisotropy (AVs), and polarization direction of faster shear wave (V_{s1}) are plotted. The x and z directions indicate the lineation and the direction normal to foliation, respectively.

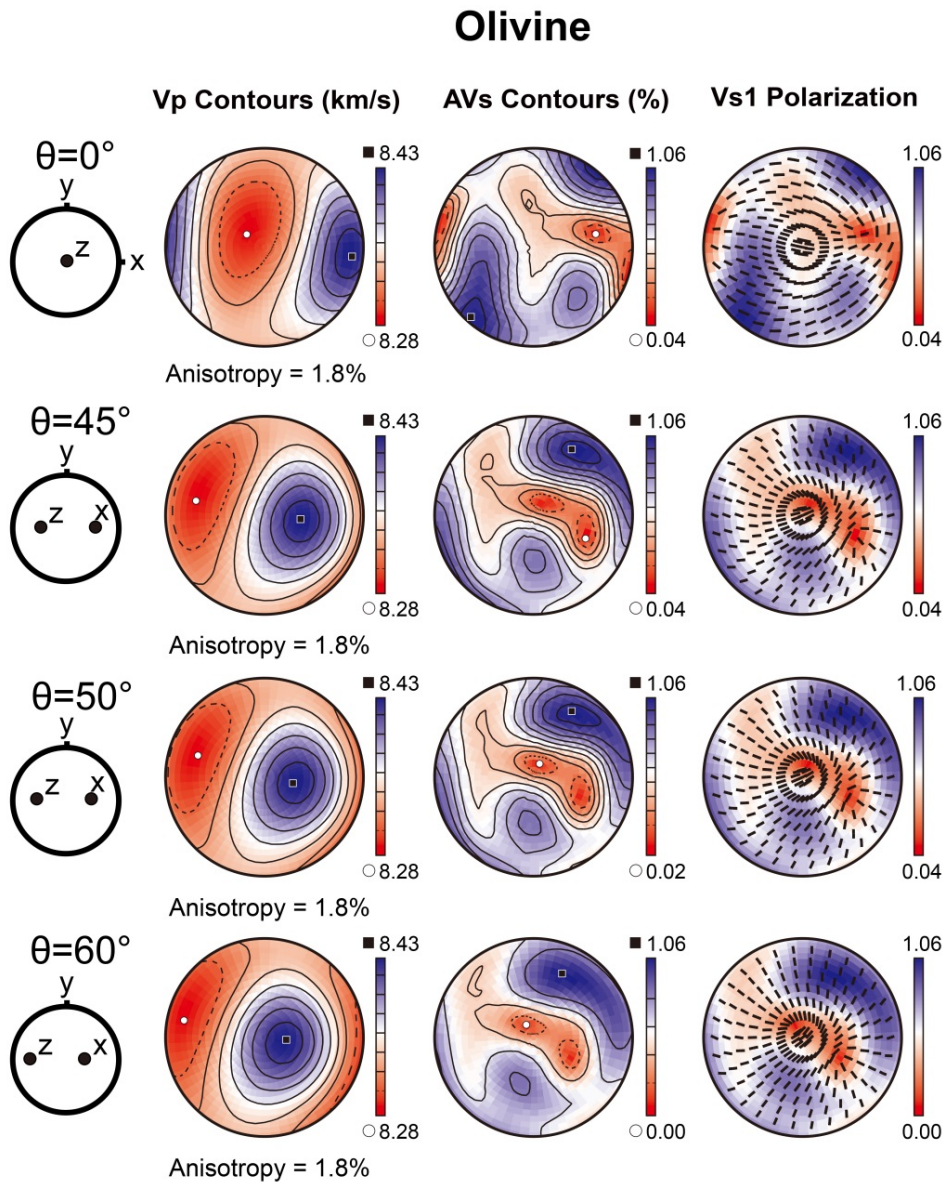


Figure 12. Effect of dip angle (θ) from $\theta=0^\circ$ to $\theta=60^\circ$ on the seismic anisotropy of amphibole considering the LPO of amphibole in sample 1194-2. P-wave velocity (V_p), S-wave anisotropy (AVs), and polarization direction of faster shear wave (V_{s1}) are plotted. The x and z directions indicate the lineation and the direction normal to foliation, respectively.

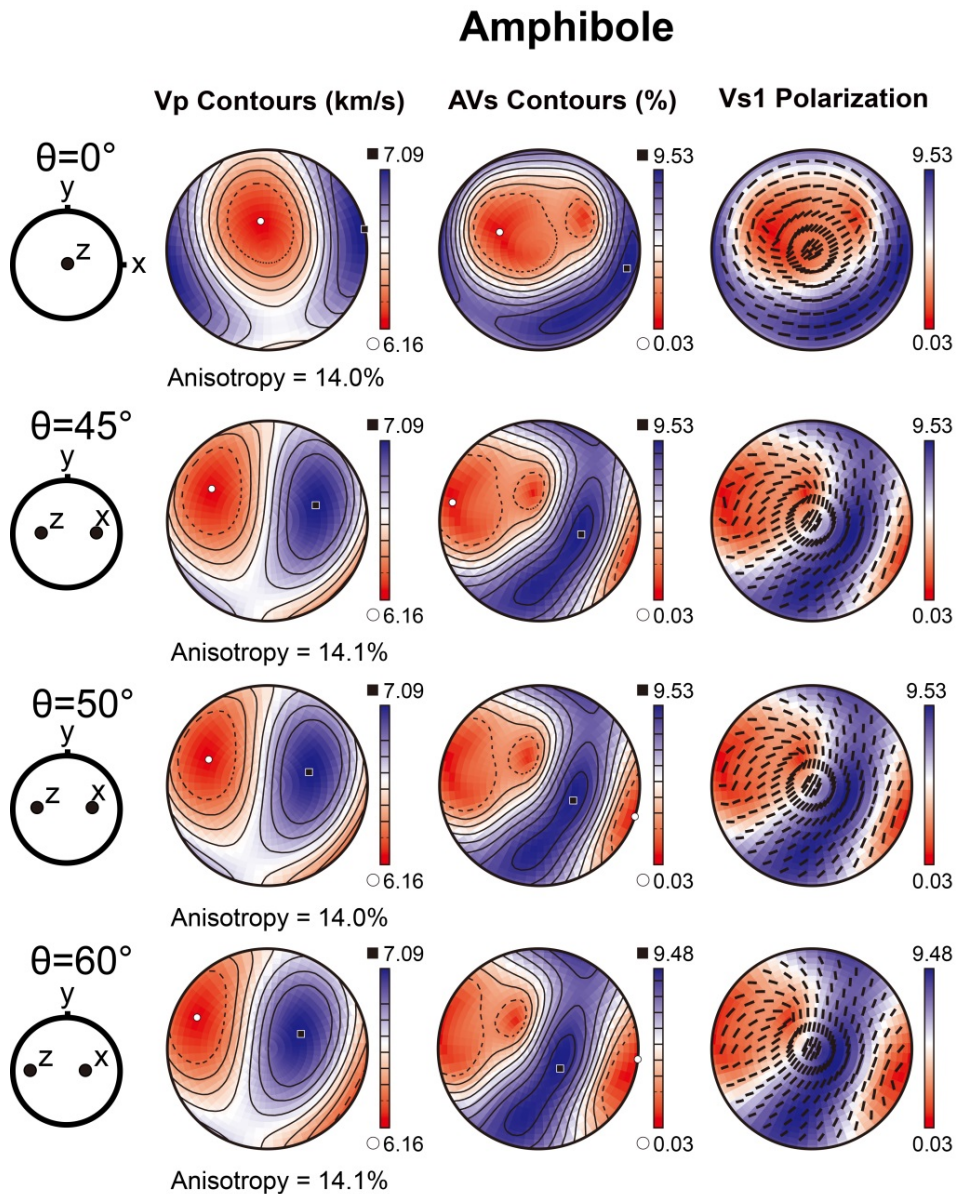


Figure 13. Effect of dip angle (θ) from $\theta=0^\circ$ to $\theta=60^\circ$ on the seismic anisotropy of chlorite considering the LPO of chlorite in sample 1194-2. P-wave velocity (V_p), S-wave anisotropy (AVs), and polarization direction of faster shear wave (V_{s1}) are plotted. The x and z directions indicate the lineation and the direction normal to foliation, respectively.

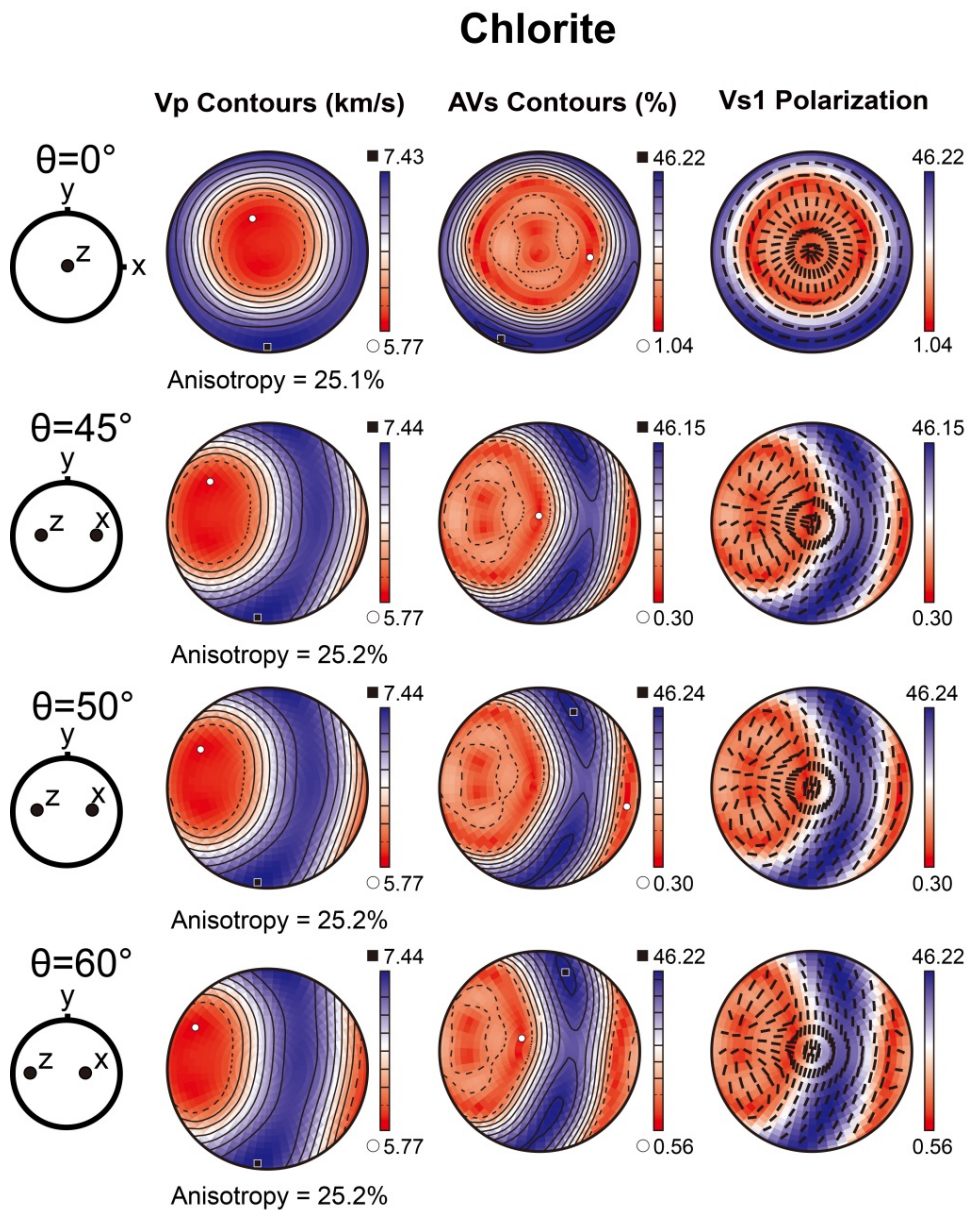


Figure 14. Effect of dip angle (θ) from $\theta=0^\circ$ to $\theta=60^\circ$ on the seismic anisotropy of whole rock considering the modal proportion and LPOs of olivine, amphibole, and chlorite in sample 1194-2. P-wave velocity (V_p), S-wave anisotropy (AVs), and polarization direction of faster shear wave (V_{s1}) are plotted. The x and z directions indicate the lineation and the direction normal to foliation, respectively.

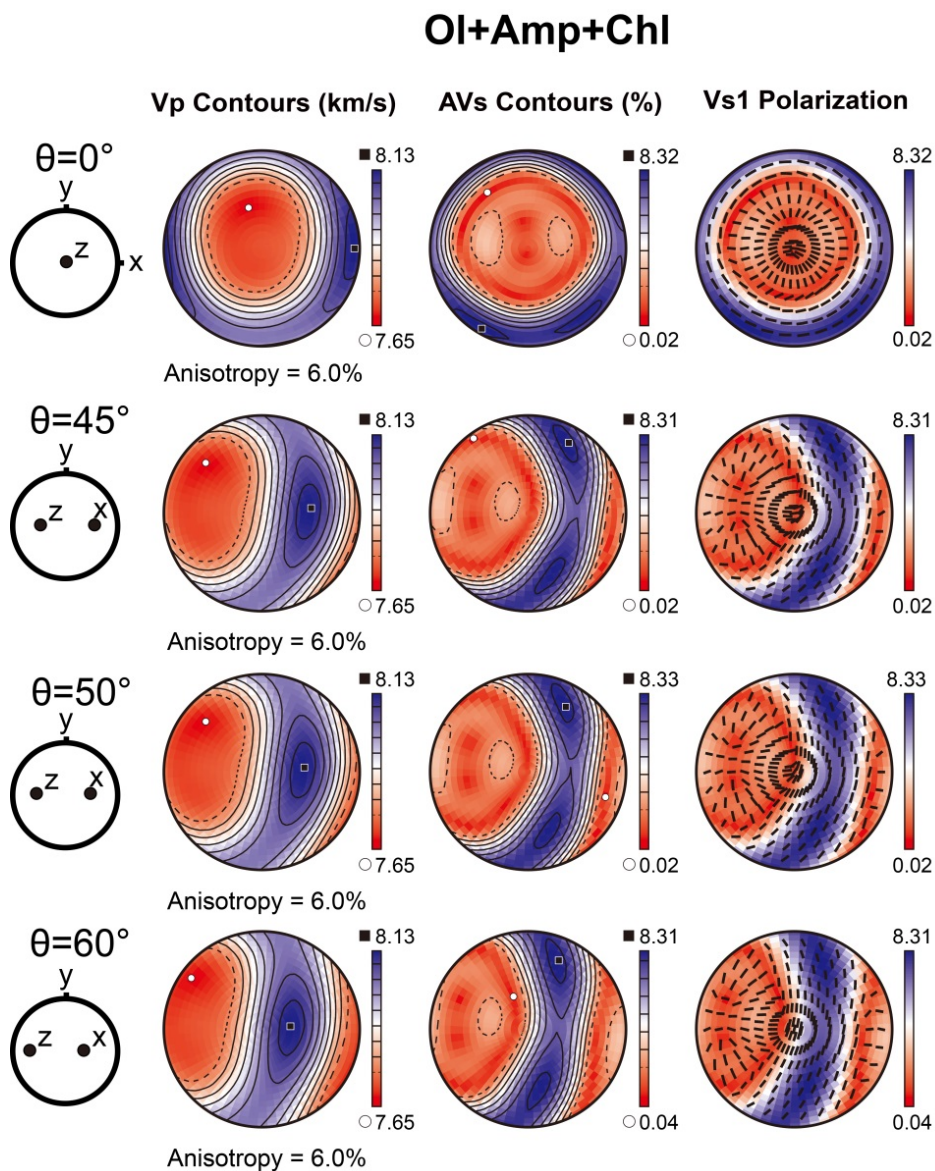
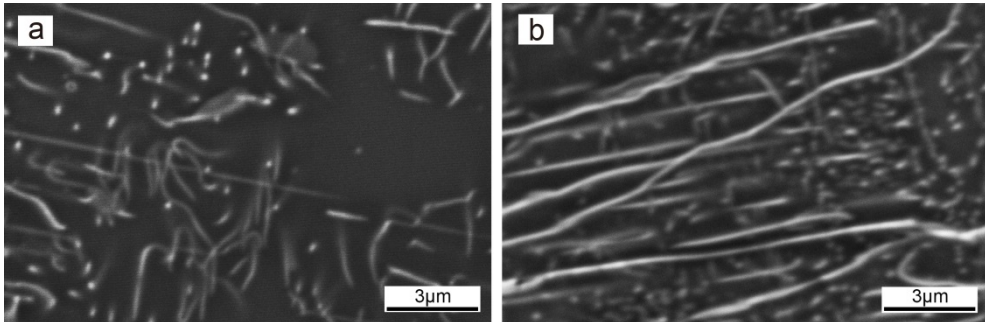
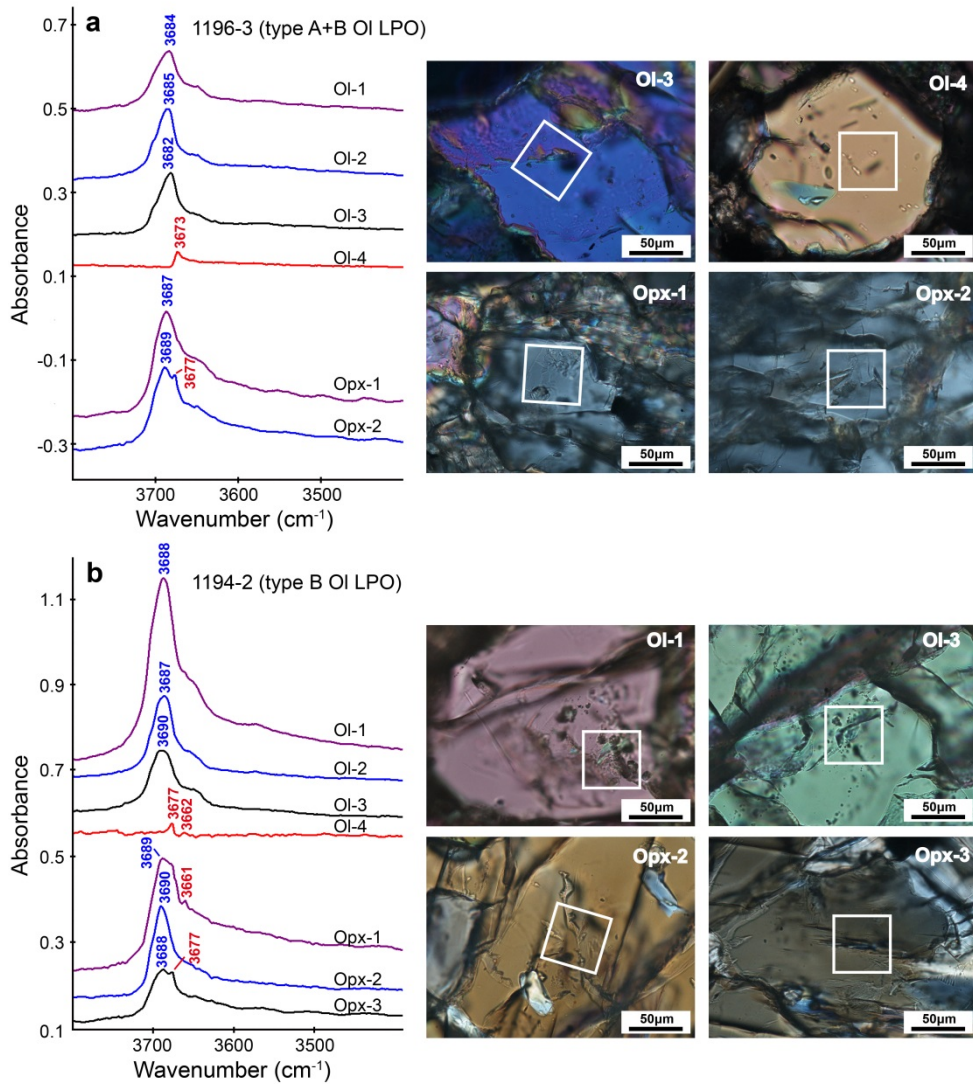


Figure 15. Dislocation microstructures of olivine in sample 1196-3 (type-A+B LPO) (a) and 1194-2 (type-B LPO) (b).



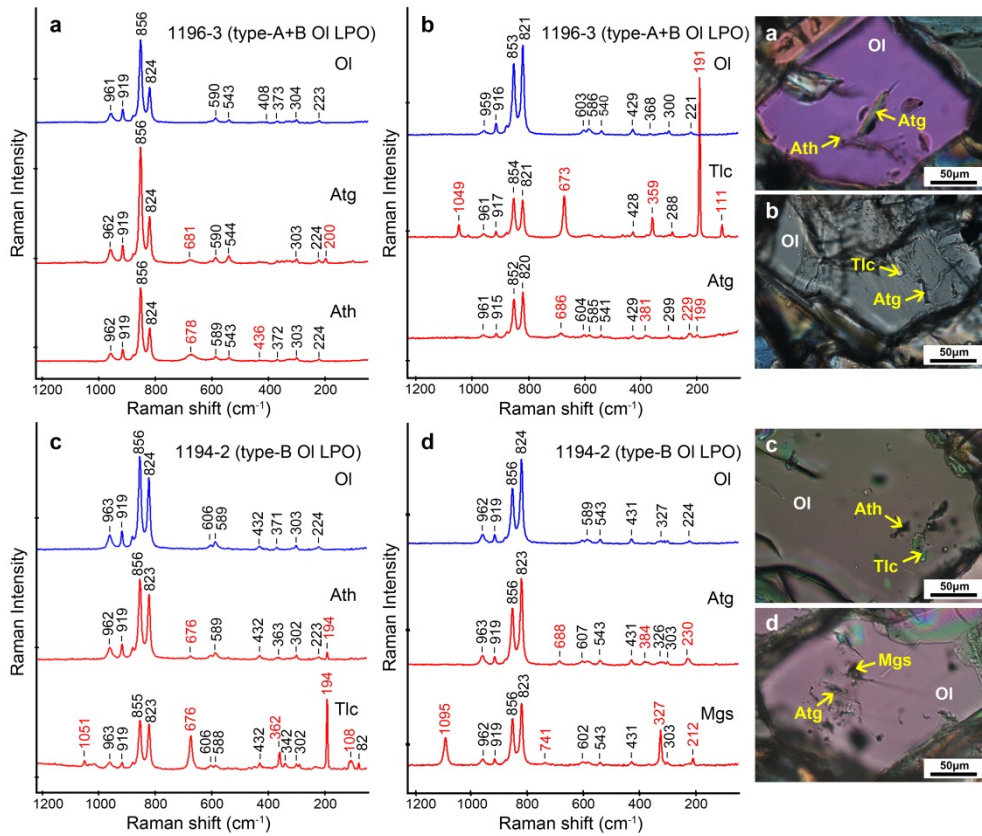
Bright lines and dots are dislocations in olivine. Scale bar is indicated in each picture.

Figure 16. FTIR spectra of olivine and orthopyroxene in samples 1196-3 (type-A+B LPO) and 1194-2 (type-B LPO).



Wavenumbers shown in blue color represent serpentine and those shown in red color represent amphibole or talc. Ol: olivine and Opx: orthopyroxene. White squares indicate area analyzed by FTIR.

Figure 17. Representative Raman spectra of host mineral (olivine) and inclusions of samples showing both type-A+B LPO (1196-3) and type-B LPO (1194-2).



Ol: olivine, Tlc: talc, Ath: anthophyllite, Atg: antigorite, and Mgs: magnesite.

Chapter 6. Discussion

6.1. Origin of the Bjørkedalen peridotites

The mineral chemistry of olivine and spinel in peridotites provides information on their origin (Arai, 1994). The high Mg# (92.4–93.1) in olivine and high Cr# (84.4–90.8) in spinel indicate that peridotites from Bjørkedalen have cratonic origin (Fig. 19). Previous studies on peridotites in WGR showed that they are mantle wedge peridotites from ultra-depleted, Archean lithospheric mantle underneath Laurentia (Beyer et al., 2012; Beyer et al., 2006; Brueckner et al., 2010; Griffin et al., 2009; Spengler et al., 2009). The extremely depleted chemical composition of the Bjørkedalen peridotites corresponds well with studies on other localities in WGR. Therefore, it can be interpreted that the Bjørkedalen peridotites are fragments of Laurentian mantle that was trapped in the Baltic crust on its subduction underneath Laurentia or consequent exhumation to crustal surface during the Scandian orogeny.

6.2. Mechanisms for fabric transition in olivine

Peridotites from Bjørkedalen showed gradual change in olivine LPOs from

type-A to type-B (Fig. 3). The type-A fabric of olivine is commonly observed in various geodynamic environments of upper mantle such as ophiolites, subduction zones, and kimberlites (Ismail and Mainprice, 1998). The type-A olivine fabric can be interpreted as a remnant fabric that resulted from long residence in the mantle wedge under low water content and low stress. Previous experimental studies proposed several mechanisms for olivine fabric transition from type-A to type-B LPO. First, It is reported that increase in confining pressure (>3 GPa) in dry olivine may induce the fabric change (Couvry et al., 2004; Jung et al., 2009b; Ohuchi et al., 2011). However, there were no index minerals of high pressure such as a diamond or coesite in the analyzed rock samples. Indeed our samples show spinel-bearing assemblage that requires equilibrium pressure to be less than 2 GPa. Therefore, pressure-induced slip transition can be excluded for the mechanism that caused type-B fabric of Bjørkedalen peridotites. The other possible explanation for B-type fabric development is the diffusion creep mechanism under high content of pyroxene (Jung et al., 2014; Sundberg and Cooper, 2008). The Bjørkedalen peridotites, however, contain less than 5% opx and no cpx within their mineral assemblage. In addition, high dislocation density observed in samples with both type-A+B and type-B LPO of olivine suggests that olivine fabric changed from type-A to type-B in dislocation creep regime. Thus the diffusion creep mechanism cannot be a possible mechanism explaining type-B fabric development of the

Bjørkedalen peridotites. Another important factor on type-B fabric development is the effect of water under high stress (Jung et al., 2006). There is a number of evidence that demonstrate the high water content in the Bjørkedalen peridotites. First, the hydrous minerals amphibole and chlorite are distributed in the samples as the stable mineral assemblage. They show consistent foliation and lineation with olivine (Figs. 2e and 2f), indicating their contemporary deformation event. Second, numerous hydrous minerals such as serpentine, talc and/or amphibole are found within the anhydrous minerals olivine and orthopyroxene by the FTIR analysis. It can be implied from the result that olivine and orthopyroxene had hosted plenty of water (–OH) within their structures before the exsolution of hydrous inclusions occurred. Last, the Raman spectroscopic study on the samples identified the sub-micrometer scale inclusions of antigorite, anthophyllite, talc, and magnesite within olivine. Anthophyllite, talc, and magnesite are common accessory minerals produced during serpentinization of olivine (Christensen, 2004).

6.3. Effect of LPO of hydrous phases on whole rock seismic anisotropy

Amphibole and chlorite may exist stably in a broad range of high temperature and high pressure (Fumagalli and Poli, 2005; Mainprice and

Ildefonse, 2009). It is estimated that those minerals comprise a considerable portion in hydrated mantle wedge and subducting slab. From our analysis it turned out that seismic anisotropy of both amphibole and chlorite is much higher than that of olivine (Table 9). It stems from two different reasons; one is the different LPO and fabric strength of the three minerals, and the other is the different anisotropic characteristics of the three single minerals. First, mean M-index increased in the order olivine ($M=0.048$), amphibole ($M=0.150$), and chlorite ($M=0.185$). The olivine aggregates within sample with type-A LPO of olivine (1190) had developed the highest M-index ($M=0.088$), resulting in AVp and maximum AVs of 7.5% and 5.2%, respectively. The samples with type-A+B and type-B LPO of olivine had relatively low M-index compared to that of the sample with type-A LPO of olivine (1190). An interesting point to note is that olivine with high content of amphibole (1196-2, ~40% Amp) developed a strong M-index (0.067) compared with other samples having low content of amphibole among the samples with type-A+B and type-B LPO of olivine ($M=0.032-0.041$). On the other hand, amphibole in Bjørkedalen peridotites showed higher M-index (0.114–0.179) than that of olivine and resulted in strong seismic anisotropy. The AVp values were up to 15.2% and the maximum AVs values were up to 11.9% for amphibole. In addition, chlorite of the Bjørkedalen peridotites developed a very strong LPO, including one with the highest M-index (1194-2, $M=0.232$). Consequently, chlorite produced

the strongest seismic anisotropy with AVp up to 25.2% and maximum AVs up to 46.2%. Second, previous studies reported that both P- and S-wave anisotropies of single crystal amphibole and chlorite are higher than that of olivine. Ismail and Mainprice (1998) showed that olivine single crystal has AVp of 24.6% and maximum AVs of 18.2%. Ko and Jung (2015) calculated that single crystal hornblende has AVp of 27.1% and maximum AVs of 30.7%. Kim and Jung (2015) showed that chlorite single crystal has AVp 35.5% and maximum AVs 76.2%. From this analysis we found that type-I LPO of amphibole produces higher AVp than AVs, although those values are lower than those of chlorite. Chlorite LPO found in this study yields the highest values of AVp and AVs among the three minerals but is especially high in AVs compared with AVp. It can be inferred that chlorite can contribute to interpret unusual high AVs observed in subduction zones (McCormack et al., 2013; Pozgay et al., 2007; Smith et al., 2001).

In addition, it is found that the hydrous minerals may contribute to change the polarization direction of the fast S-wave (V_{s1}) in the peridotites (Fig. 19). The dipping angle (θ) of the slab may reflect the angle of the downward movement of the mantle wedge considering the 2-dimensional corner flow. For a horizontal flow, olivine with type-B fabric (1194-2) showed a V_{s1} polarization direction subparallel to lineation or flow direction (trench-normal) for a vertically propagating S-wave (Fig 11). It is contrary to the previous studies that showed trench-parallel V_{s1} polarization direction of

vertically propagating S-wave for the type-B olivine LPO (Jung and Karato, 2001b; Jung et al., 2009b; Lee and Jung, 2015). This disparity results from the random distribution of [100] axes of olivine in sample 1194-2, compared with typical type-B olivine LPOs that show strong concentration of [100] axes in the direction normal to lineation on the foliation plane. Although the trench-normal polarization direction of the Vs1 for olivine changes gradually to the trench-parallel direction with increasing dipping angle from $\theta=45^\circ$ to $\theta=60^\circ$, the amplitude of the AVs remains very small ($\sim 0.3\%$ at $\theta=60^\circ$) that olivine alone cannot contribute to strong trench-parallel seismic anisotropy observed in subduction zones. Amphibole with type-I LPO results in oblique Vs1 polarization direction nearly tilted 45° to the y (trench-direction) for the vertically propagating S-waves considering the horizontal flow and the amplitude of the AVs is small $\sim 1.6\%$ (Fig 12). If the dipping angle of the slab becomes 45° the polarization direction of the vertically propagating Vs1 changes closer to the trench-parallel direction. Also the AVs amplitude changes to the higher values ($\sim 4\%$ at $\theta=45^\circ$ and $\sim 7\%$ at $\theta=60^\circ$). Chlorite LPO makes small AVs ($\sim 5\%$) and nearly horizontal (trench-normal) Vs1 polarization direction for the vertically propagating S-waves in horizontal flow model (Fig 13). It changes to vertical direction (trench-parallel) when dipping angle of flow becomes $\theta=50^\circ$ and the AVs values changes to higher values ($\sim 9\%$ at $\theta=50^\circ$ and $\sim 20\%$ at $\theta=60^\circ$) as well. The vertically propagating Vs1 shows mixed trench-normal and trench-

parallel polarization direction until $\theta=45^\circ$ and it changes to trench-parallel direction from the dipping angle $\theta=50^\circ$. The angle calculated in this paper where Vs1 polarization direction of the vertically propagating S-wave changes to trench-parallel direction is nearly consistent with previous studies on amphibole (Ko and Jung, 2015) and chlorite (Kim and Jung, 2015). The change of the Vs1 polarization direction was more dramatic in the changing dipping angle for chlorite than amphibole. The whole rock result considering all the three minerals showed that the seismic anisotropy pattern of the whole rock follows that of the chlorite the most (Fig. 14). The Vs1 polarization direction of the vertically propagating S-waves through the whole rock changed from the horizontal or trench-normal ($\theta=0^\circ$) to mixed ($\theta=45^\circ$ and $\theta=50^\circ$) and trench-parallel ($\theta=60^\circ$). Although the whole rock seismic anisotropy pattern follows that of chlorite the most, the trench-normal component of Vs1 polarization direction of vertically propagating S-wave which was shown in the dipping angle up to 50° may reflect that of the most abundant mineral, olivine ($\sim 80\%$). In addition, the amplitude of the AVs of the vertically propagating S-waves for the whole rock changed from small ($\sim 1\%$ at $\theta=0^\circ$) to large ($\sim 3\%$ at $\theta=60^\circ$) with increasing dipping angle. The AVs amplitude at $\theta=60^\circ$ ($\sim 3\%$) is much higher compared with olivine-only case ($\sim 0.3\%$).

Overall, our results suggest that the existence of the strong LPO of hydrous minerals such as amphibole and chlorite produces a strong seismic

anisotropy in a peridotite. Also, it can be inferred from this study that hydrous minerals amphibole and chlorite contribute to strong trench-parallel seismic anisotropy at steeply dipping subduction zone ($\theta=45^\circ$ for amphibole and $\theta=50^\circ$ for chlorite).

Figure 18. Olivine–spinel mantle array (OSMA) trend (Arai, 1994) showing cratonic origin of the Bjørkedalen peridotites. Green squares indicate composition of olivine and spinel Bjørkedalen peridotites. Modified after Clos et al. (2014).

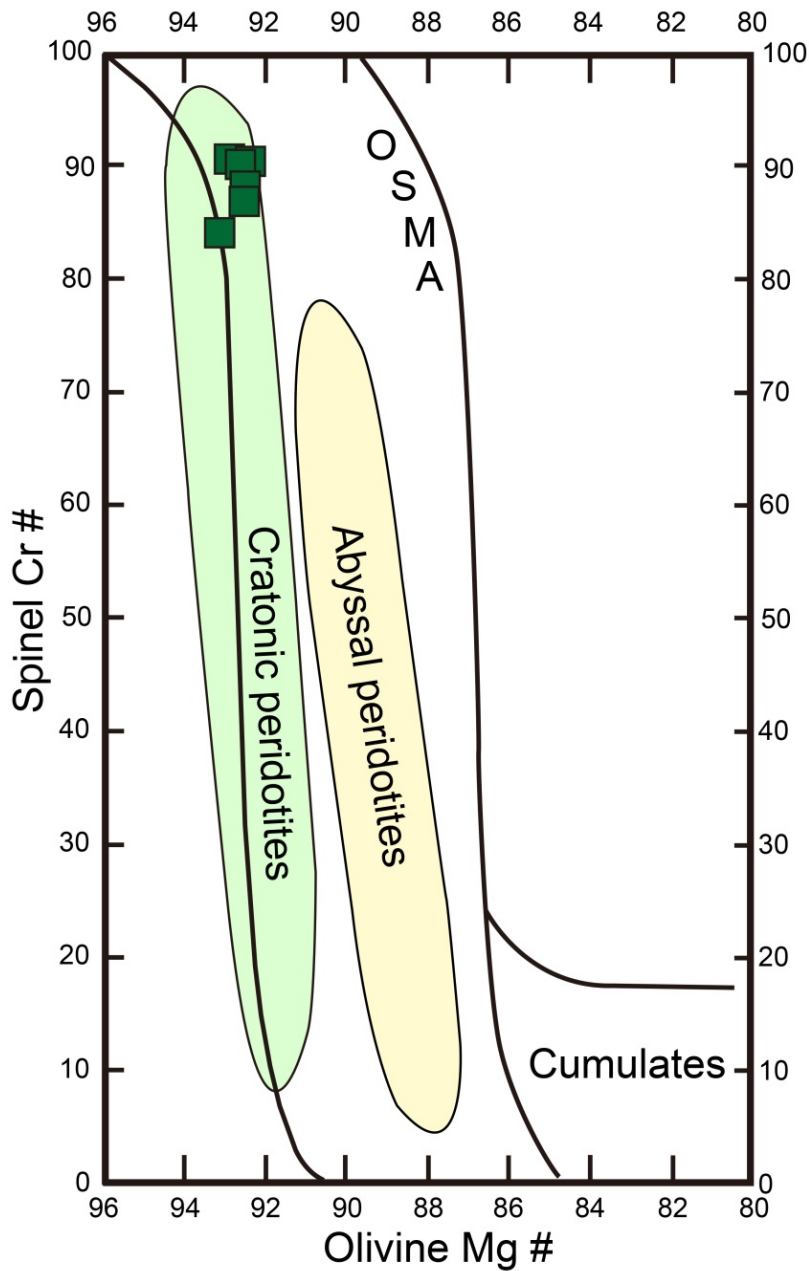


Figure 19. Effect of dip angle (θ) on the seismic anisotropy of olivine, amphibole, chlorite, and whole rock considering the LPOs of the three minerals within sample 1194-2. (a) seismic anisotropy for the horizontal flow. (b) seismic anisotropy for the flow dipping at 60° to the west from the horizontal flow. The x and z directions indicate the lineation and the direction normal to foliation, respectively.

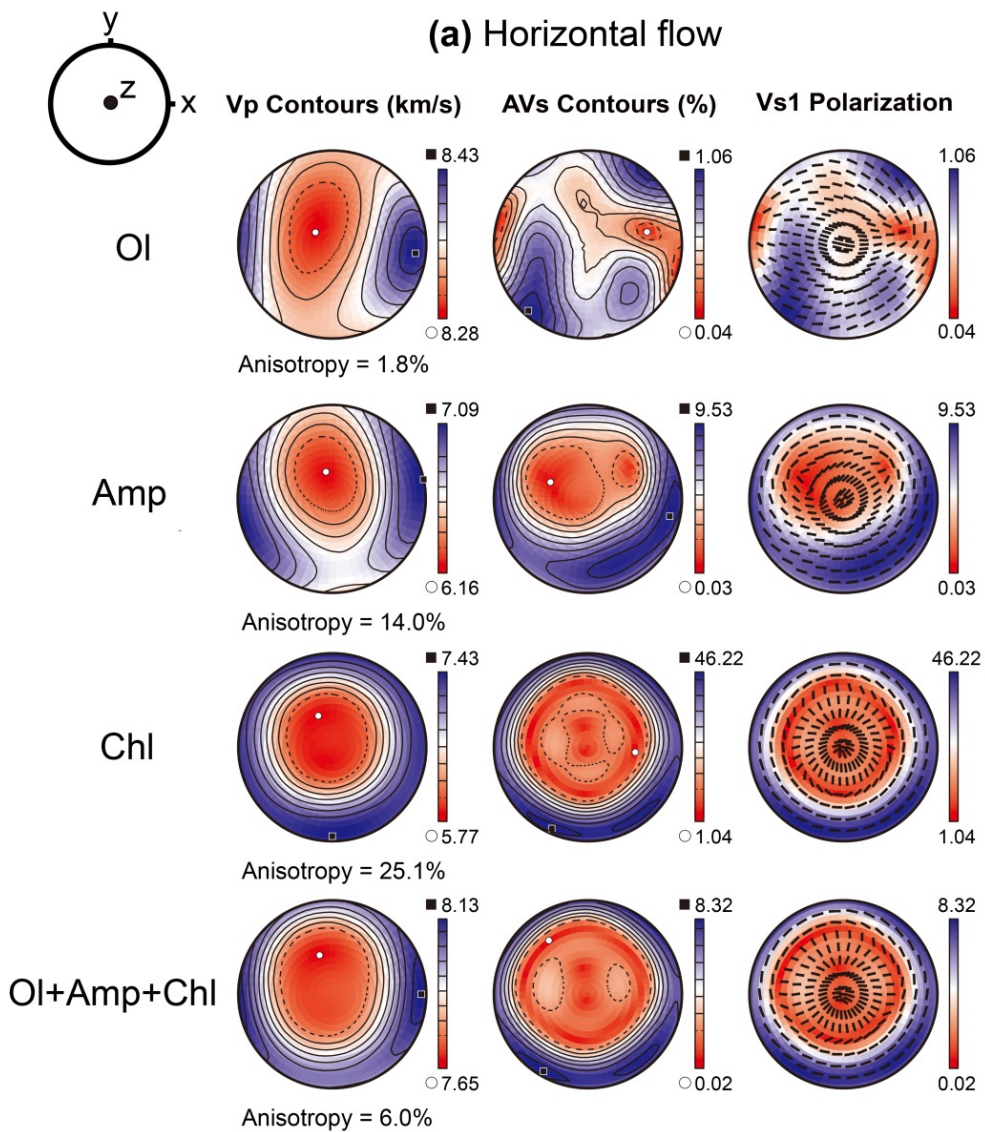
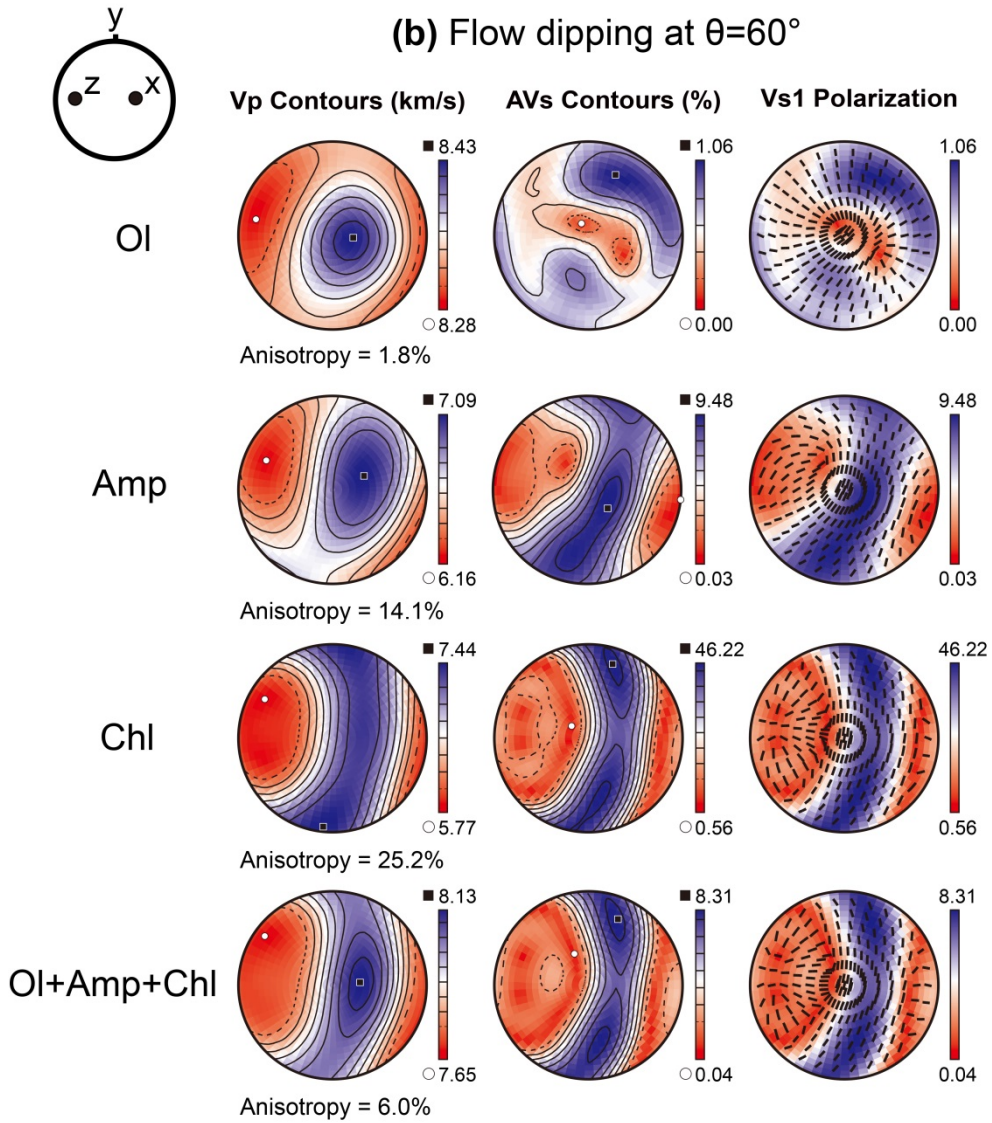


Figure 19. Continued (Figure caption is in page 49).



Chapter 7. Conclusion

In this study, gradually changing olivine LPO in peridotites from Bjørkedalen from type-A to type-B was observed. One sample (1190) showed type-A LPO of olivine in which [100] axes are aligned subparallel to lineation and [010] axes subnormal to foliation. The other two samples (1194-1 and 1194-2) showed type-B LPO of olivine in which [010] axes are aligned subnormal to foliation and [001] axes are aligned subparallel to lineation. Other samples (1193, 1196-1, 1196-2, and 1196-3) showed LPO of olivine in the midway of type-A and type-B. Each sample contained varying amount of amphibole (0–41%) and chlorite (0.2–10%) in modal composition. Amphibole LPOs were similar in all the analyzed samples (1196-1, 1196-2, 1196-3, 1194-1, and 1194-2). Amphibole grains were aligned with their [001] axes subparallel to lineation and [100] axes subnormal to foliation (type-I LPO). All the analyzed samples showed similar LPO of chlorite (1196-3 and 1194-2). The [100] axes of chlorite were aligned subparallel to lineation and [001] axes were subnormal to foliation.

The calculated seismic anisotropy of the studied peridotite samples showed that amphibole and chlorite in a peridotite have a profound effect on the seismic anisotropy of whole rock. In this study, the P- and S-wave anisotropies of amphibole reached 15.2% and 11.9%, respectively. Those

values of chlorite were up to 25.2% and 46.2%, respectively. In addition, both amphibole and chlorite in a hydrated peridotite change the polarization of the V_{s1} for vertically propagating S-waves from the trench-normal to trench-parallel direction depending on the dipping angle of mantle flow. It is concluded that although olivine is the major mineral making up peridotites, a relatively small amount of amphibole and chlorite can contribute to seismic anisotropy of the whole rock significantly.

References

- Abramson, E., Brown, J., Slutsky, L., and Zaug, J., 1997, The elastic constants of San Carlos olivine to 17 GPa: *Journal of Geophysical Research: Solid Earth* (1978–2012), v. 102, no. B6, p. 12253-12263.
- Aleksandrov, K., and Ryzhova, T., 1961, The elastic properties of rock forming minerals, pyroxenes and amphiboles: *Bull. Acad. Sci. USSR, Geophys. Ser.*, v. 9, p. 871-875.
- Arai, S., 1994, Characterization of spinel peridotites by olivine-spinel compositional relationships: review and interpretation: *Chemical geology*, v. 113, no. 3, p. 191-204.
- Beyer, E. E., 2006, Transformation of Archaean Lithospheric Mantle by Refertilization: Evidence from Exposed Peridotites in the Western Gneiss Region, Norway: *Journal of Petrology*, v. 47, no. 8, p. 1611-1636.
- Beyer, E. E., Brueckner, H. K., Griffin, W. L., and O'Reilly, S. Y., 2012, Laurentian Provenance of Archean Mantle Fragments in the Proterozoic Baltic Crust of the Norwegian Caledonides: *Journal of Petrology*, v. 53, no. 7, p. 1357-1383.
- Beyer, E. E., Griffin, W. L., and O'REILLY, S. Y., 2006, Transformation of Archaean lithospheric mantle by refertilization: evidence from exposed peridotites in the Western Gneiss Region, Norway: *Journal*

- of Petrology, v. 47, no. 8, p. 1611-1636.
- Brueckner, H., and Van Roermund, H., 2004, Dunk tectonics: A multiple subduction/eduction model for the evolution of the Scandinavian Caledonides. *Tectonics* 23, TC2004.
- Brueckner, H. K., Carswell, D. A., Griffin, W. L., Medaris, L. G., Van Roermund, H. L. M., and Cuthbert, S. J., 2010, The mantle and crustal evolution of two garnet peridotite suites from the Western Gneiss Region, Norwegian Caledonides: An isotopic investigation: *Lithos*, v. 117, no. 1-4, p. 1-19.
- Carswell, D., 1986, The metamorphic evolution of Mg-Cr type Norwegian garnet peridotites: *Lithos*, v. 19, no. 3, p. 279-297.
- Christensen, N. I., 2004, Serpentinites, Peridotites, and Seismology: *International Geology Review*, v. 46, no. 9, p. 795-816.
- Clos, F., Gilio, M., and van Roermund, H. L. M., 2014, Fragments of deeper parts of the hanging wall mantle preserved as orogenic peridotites in the central belt of the Seve Nappe Complex, Sweden: *Lithos*, v. 192-195, p. 8-20.
- Couvy, H., Frost, D. J., Heidelbach, F., Nyilas, K., Ungár, T., Mackwell, S., and Cordier, P., 2004, Shear deformation experiments of forsterite at 11 GPa - 1400°C in the multianvil apparatus: *European Journal of Mineralogy*, v. 16, no. 6, p. 877-889.
- Cuthbert, S., Carswell, D., Krogh-Ravna, E., and Wain, A., 2000, Eclogites

- and eclogites in the Western Gneiss region, Norwegian Caledonides:
Lithos, v. 52, no. 1, p. 165-195.
- Frese, K., Trommsdorff, V., and Kunze, K., 2003, Olivine [100] normal to
foliation: lattice preferred orientation in prograde garnet peridotite
formed at high H₂O activity, Cima di Gagnone (Central Alps):
Contributions to Mineralogy and Petrology, v. 145, no. 1, p. 75-86.
- Fumagalli, P., and Poli, S., 2005, Experimentally determined phase relations
in hydrous peridotites to 6· 5 GPa and their consequences on the
dynamics of subduction zones: Journal of Petrology, v. 46, no. 3, p.
555-578.
- Gifkins, R. C., 1970, Optical microscopy of metals, American Elsevier.
- Griffin, W., O'Reilly, S. Y., Afonso, J. C., and Begg, G., 2009, The
composition and evolution of lithospheric mantle: a re-evaluation
and its tectonic implications: Journal of Petrology, v. 50, no. 7, p.
1185-1204.
- Hacker, B. R., Andersen, T. B., Johnston, S., Kylander-Clark, A. R. C.,
Peterman, E. M., Walsh, E. O., and Young, D., 2010, High-
temperature deformation during continental-margin subduction &
exhumation: The ultrahigh-pressure Western Gneiss Region of
Norway: Tectonophysics, v. 480, no. 1-4, p. 149-171.
- Hirauchi, K.-i., Michibayashi, K., Ueda, H., and Katayama, I., 2010, Spatial
variations in antigorite fabric across a serpentinite subduction

- channel: Insights from the Ohmachi Seamount, Izu-Bonin frontal arc:
Earth and Planetary Science Letters, v. 299, no. 1-2, p. 196-206.
- Ismail, W. B., and Mainprice, D., 1998, An olivine fabric database: an
overview of upper mantle fabrics and seismic anisotropy:
Tectonophysics, v. 296, no. 1, p. 145-157.
- Jung, H., 2009, Deformation fabrics of olivine in Val Malenco peridotite
found in Italy and implications for the seismic anisotropy in the
upper mantle: Lithos, v. 109, no. 3-4, p. 341-349.
- Jung, H., 2011, Seismic anisotropy produced by serpentine in mantle wedge:
Earth and Planetary Science Letters, v. 307, no. 3-4, p. 535-543.
- Jung, H., and Karato, S.-I., 2001a, Effects of water on dynamically
recrystallized grain-size of olivine: Journal of Structural Geology, v.
23, no. 9, p. 1337-1344.
- Jung, H., and Karato, S.-I., 2001b, Water-induced fabric transitions in
olivine: Science, v. 293, no. 5534, p. 1460-1463.
- Jung, H., Katayama, I., Jiang, Z., Hiraga, T., and Karato, S.-I., 2006, Effect
of water and stress on the lattice-preferred orientation of olivine:
Tectonophysics, v. 421, no. 1, p. 1-22.
- Jung, H., Lee, J., Ko, B., Jung, S., Park, M., Cao, Y., and Song, S., 2013,
Natural type-C olivine fabrics in garnet peridotites in North Qaidam
UHP collision belt, NW China: Tectonophysics, v. 594, p. 91-102.
- Jung, H., Mo, W., and Choi, S. H., 2009a, Deformation microstructures of

- olivine in peridotite from Spitsbergen, Svalbard and implications for seismic anisotropy: *Journal of Metamorphic Geology*, v. 27, no. 9, p. 707-720.
- Jung, H., Mo, W., and Green, H. W., 2009b, Upper mantle seismic anisotropy resulting from pressure-induced slip transition in olivine: *Nature Geoscience*, v. 2, no. 1, p. 73-77.
- Jung, S., Jung, H., and Austrheim, H., 2014, Characterization of olivine fabrics and mylonite in the presence of fluid and implications for seismic anisotropy and shear localization: *Earth, Planets and Space*, v. 66, no. 1, p. 46.
- Karato, S.-i., Jung, H., Katayama, I., and Skemer, P., 2008, Geodynamic significance of seismic anisotropy of the upper mantle: new insights from laboratory studies: *Annu. Rev. Earth Planet. Sci.*, v. 36, p. 59-95.
- Karato, S., 1987, Scanning electron microscope observation of dislocations in olivine: *Physics and Chemistry of Minerals*, v. 14, no. 3, p. 245-248.
- Katayama, I., Hirauchi, K., Michibayashi, K., and Ando, J., 2009, Trench-parallel anisotropy produced by serpentine deformation in the hydrated mantle wedge: *Nature*, v. 461, no. 7267, p. 1114-1117.
- Katayama, I., Jung, H., and Karato, S.-i., 2004, New type of olivine fabric from deformation experiments at modest water content and low

- stress: *Geology*, v. 32, no. 12, p. 1045-1048.
- Katayama, I., Karato, S.-i., and Brandon, M., 2005, Evidence of high water content in the deep upper mantle inferred from deformation microstructures: *Geology*, v. 33, no. 7, p. 613.
- Kim, D., and Jung, H., 2015, Deformation microstructures of olivine and chlorite in chlorite peridotites from Almklovdalen in the Western Gneiss Region, southwest Norway, and implications for seismic anisotropy: *International Geology Review*, v. 57, no. 5-8, p. 650-668.
- Ko, B., and Jung, H., 2015, Crystal preferred orientation of an amphibole experimentally deformed by simple shear: *Nat Commun*, v. 6, p. 6586.
- Kohlstedt, D., Goetze, C., Durham, W., and Vander Sande, J., 1976, New technique for decorating dislocations in olivine: *Science*, v. 191, no. 4231, p. 1045-1046.
- Krogh, E. J., 1977, Evidence of Precambrian continent-continent collision in Western Norway: *Nature*, v. 267, p. 17-19.
- Kylander-Clark, A., Hacker, B., Johnson, C., Beard, B., Mahlen, N., and Lapen, T., 2007, Timing of multi-stage metamorphism during ultrahigh-pressure continental subduction and exhumation: Lu/Hf and Sm/Nd geochronology in western Norway: *Chemical Geology*, v. 232, p. 137-154.
- Kylander-Clark, A., Hacker, B., and Mattinson, J., 2008, Slow exhumation

- of UHP terranes: titanite and rutile ages of the Western Gneiss Region, Norway: *Earth and Planetary Science Letters*, v. 272, no. 3, p. 531-540.
- Lapen, T. J., Medaris, L. G., Beard, B. L., and Johnson, C. M., 2009, The Sandvik peridotite, Gurskøy, Norway: Three billion years of mantle evolution in the Baltica lithosphere: *Lithos*, v. 109, no. 3-4, p. 145-154.
- Lee, J., and Jung, H., 2015, Lattice-preferred orientation of olivine found in diamond-bearing garnet peridotites in Finsch, South Africa and implications for seismic anisotropy: *Journal of Structural Geology*, v. 70, p. 12-22.
- Linckens, J., Herwegh, M., Müntener, O., and Mercolli, I., 2011, Evolution of a polymineralic mantle shear zone and the role of second phases in the localization of deformation: *Journal of Geophysical Research: Solid Earth (1978–2012)*, v. 116, no. B6.
- Möckel, J. R., 1969, Structural petrology of the garnet-peridotite of Alpe Arami (Ticino, Switzerland): *Leidse Geologische Mededelingen*, v. 42, no. 1, p. 61-130.
- Mainprice, D., 1990, A FORTRAN program to calculate seismic anisotropy from the lattice preferred orientation of minerals: *Computers & Geosciences*, v. 16, no. 3, p. 385-393.
- Mainprice, D., and Ildefonse, B., 2009, Seismic anisotropy of subduction

zone minerals—contribution of hydrous phases, Subduction zone geodynamics, Springer, p. 63-84.

McCormack, K., Wirth, E. A., and Long, M. D., 2013, B-type olivine fabric and mantle wedge serpentinization beneath the Ryukyu arc: *Geophysical Research Letters*, v. 40, no. 9, p. 1697-1702.

Mehl, L., Hacker, B. R., Hirth, G., and Kelemen, P. B., 2003, Arc-parallel flow within the mantle wedge: Evidence from the accreted Talkeetna arc, south central Alaska: *Journal of Geophysical Research: Solid Earth (1978–2012)*, v. 108, no. B8.

Miller, G. H., Rossman, G. R., and Harlow, G. E., 1987, The natural occurrence of hydroxide in olivine: *Physics and Chemistry of Minerals*, v. 14, no. 5, p. 461-472.

Mizukami, T., Wallis, S. R., and Yamamoto, J., 2004, Natural examples of olivine lattice preferred orientation patterns with a flow-normal a-axis maximum: *Nature*, v. 427, no. 6973, p. 432-436.

Morales, L. F. G., Mainprice, D., and Boudier, F., 2013, The influence of hydrous phases on the microstructure and seismic properties of a hydrated mantle rock: *Tectonophysics*, v. 594, p. 103-117.

Nishii, A., Wallis, S. R., Mizukami, T., and Michibayashi, K., 2011, Subduction related antigorite CPO patterns from forearc mantle in the Sanbagawa belt, southwest Japan: *Journal of Structural Geology*, v. 33, no. 10, p. 1436-1445.

- Ohuchi, T., Kawazoe, T., Nishihara, Y., Nishiyama, N., and Irifune, T., 2011, High pressure and temperature fabric transitions in olivine and variations in upper mantle seismic anisotropy: *Earth and Planetary Science Letters*, v. 304, no. 1-2, p. 55-63.
- Panozzo, R., 1984, Two-dimensional strain from the orientation of lines in a plane: *Journal of Structural Geology*, v. 6, no. 1, p. 215-221.
- Park, M., Jung, H., and Kil, Y., 2014, Petrofabrics of olivine in a rift axis and rift shoulder and their implications for seismic anisotropy beneath the Rio Grande rift: *Island Arc*, v. 23, no. 4, p. 299-311.
- Park, Y., and Jung, H., 2015, Deformation microstructures of olivine and pyroxene in mantle xenoliths in Shanwang, eastern China, near the convergent plate margin, and implications for seismic anisotropy: *International Geology Review*, v. 57, no. 5-8, p. 629-649.
- Pozgay, S., Wiens, D., Conder, J., Shiobara, H., and Sugioka, H., 2007, Complex mantle flow in the Mariana subduction system: evidence from shear wave splitting: *Geophysical Journal International*, v. 170, no. 1, p. 371-386.
- Roberts, D., 2003, The Scandinavian Caledonides: event chronology, palaeogeographic settings and likely modern analogues: *Tectonophysics*, v. 365, no. 1, p. 283-299.
- Roberts, D., and Gee, D., 1985, An introduction to the structure of the Scandinavian Caledonides: *The Caledonide orogen—Scandinavia and*

related areas, v. 1, p. 55-68.

Root, D., Hacker, B., Gans, P., Ducea, M., Eide, E., and Mosenfelder, J., 2005, Discrete ultrahigh-pressure domains in the Western Gneiss Region, Norway: implications for formation and exhumation: *Journal of Metamorphic Geology*, v. 23, no. 1, p. 45-61.

Sawaguchi, T., 2004, Deformation history and exhumation process of the Horoman Peridotite Complex, Hokkaido, Japan: *Tectonophysics*, v. 379, no. 1-4, p. 109-126.

Skemer, P., Katayama, I., Jiang, Z., and Karato, S.-i., 2005, The misorientation index: Development of a new method for calculating the strength of lattice-preferred orientation: *Tectonophysics*, v. 411, no. 1, p. 157-167.

Skemer, P., Katayama, I., and Karato, S.-i., 2006, Deformation fabrics of the Cima di Gagnone peridotite massif, Central Alps, Switzerland: evidence of deformation at low temperatures in the presence of water: *Contributions to Mineralogy and Petrology*, v. 152, no. 1, p. 43-51.

Skogby, H., and Rossman, G. R., 1991, The intensity of amphibole OH bands in the infrared absorption spectrum: *Physics and Chemistry of Minerals*, v. 18, no. 1, p. 64-68.

Smith, G. P., Wiens, D. A., Fischer, K. M., Dorman, L. M., Webb, S. C., and Hildebrand, J. A., 2001, A complex pattern of mantle flow in the Lau backarc: *Science*, v. 292, no. 5517, p. 713-716.

- Spengler, D., Brueckner, H. K., van Roermund, H. L., Drury, M. R., and Mason, P. R., 2009, Long-lived, cold burial of Baltica to 200 km depth: *Earth and Planetary Science Letters*, v. 281, no. 1, p. 27-35.
- Stephens, M. B., and Gee, D. G., 1989, Terranes and polyphase accretionary history in the Scandinavian Caledonides: *Geological Society of America Special Papers*, v. 230, p. 17-30.
- Sundberg, M., and Cooper, R. F., 2008, Crystallographic preferred orientation produced by diffusional creep of harzburgite: effects of chemical interactions among phases during plastic flow: *Journal of Geophysical Research: Solid Earth (1978–2012)*, v. 113, no. B12.
- Tasaka, M., Michibayashi, K., and Mainprice, D., 2008, B-type olivine fabrics developed in the fore-arc side of the mantle wedge along a subducting slab: *Earth and Planetary Science Letters*, v. 272, no. 3-4, p. 747-757.
- Toxopeus, J. B., 1976, Petrofabrics, microtextures and dislocation substructures of olivine in a peridotite mylonite (Alpe Arami, Switzerland): *Leidse Geol. Meded.*, v. 51, p. 1-36.
- Toxopeus, J. B., 1977, Fabric development of olivine in a peridotite mylonite: *Tectonophysics*, v. 39, no. 1, p. 55-71.
- Witt-Eickschen, G., and Seck, H. A., 1991, Solubility of Ca and Al in orthopyroxene from spinel peridotite: an improved version of an empirical geothermometer: *Contributions to Mineralogy and*

Petrology, v. 106, no. 4, p. 431-439.

국문요약

본 연구에서는 노르웨이 남서부 비에르케달렌 지역에서 산출된 맨틀 감람암에 들어있는 감람석, 각섬석, 그리고 녹니석의 격자선호방향을 SEM/EBSD (Electron Backscattered Diffraction) 기법을 사용하여 분석하였다. 연구 시료는 엽리가 잘 발달한 반상 조직의 감람암으로, 주로 감람석 (59–99%), 각섬석 (0–41%), 녹니석 (0.2–10%)으로 이루어져 있고 부수 광물로는 사방휘석과 크로마이트가 들어있다. 감람석의 격자선호방향은 type-A, type-B, 그리고 중간적인 type-A+B LPO를 나타내었다. 각섬석의 격자선호방향은 5개 시료에서 모두 [001]축이 선구조에 평행하고 [100]축이 엽리에 수직한 type-I으로 분석되었다. 녹니석은 2개 시료에서 모두 [100]축이 선구조에 평행하고 [001]축이 엽리에 수직한 격자선호방향을 보여주었다. 감람석과 사방휘석 내부에 들어있는 포유물들에 대해 Fourier Transformation Infrared Spectroscopy (FTIR) 분석을 한 결과 포유물들이 사문석, 활석, 각섬석 광물들임을 발견하였다. 또한 라만 분광기를 사용한 시료 분석을 통해 감람석 내부에 들어있는 작은 포유물들이 위에 기술한 수화광물들과 마스네사이트임을 확인하였다. 위

포유광물들은 감람석과 사방휘석이 물을 많이 포함하고 있었음을 지시한다. 따라서 비에르케달렌 감람암은 높은 물 함량과 비교적 높은 응력 조건에서 변형되어 감람석의 격자선호방향이 변화하였음을 지시한다. 감람석, 각섬석, 그리고 녹니석의 탄성계수, 밀도, 그리고 격자선호방향을 사용하여 지진파 비등방성을 계산하였더니 녹니석, 각섬석, 감람석 순으로 지진파의 비등방성이 크게 나타났다. 또한 각섬석과 녹니석은 맨틀의 흐름이 각각 45° 와 50° 이상의 경사각을 가질 때 지표면에 수직하게 전파하는 전단파에 대해 해구에 평행한 빠른 전단파의 편광방향을 만들 수 있음을 보여주었다. 본 연구는 섭입대 등 물이 많은 상부 맨틀 환경에서 감람암이 변형되면 각섬석과 녹니석이 격자선호방향을 형성하여 이 암석을 통과하는 지진파의 비등방성에 큰 영향을 준다는 것을 보여주었다.

주요어: 감람석, 각섬석, 녹니석, 격자선호방향, 지진파 비등방성, 비에르케달렌

학번: 2013-22966